

Interplay between powder catchment efficiency and layer height in self-stabilized laser metal deposition

Simone Donadello^{a,b}, Valentina Furlan^a, Ali Gökhan Demir^a, Barbara Previtali^a

^a*Department of Mechanical Engineering, Politecnico di Milano, Via La Masa 1, 20156 Milan, Italy*

^b*Istituto Nazionale di Ricerca Metrologica, INRIM, Strada delle Cacce 91, 10135 Turin, Italy*

Abstract

In laser metal deposition (LMD) the height of the deposited track can vary within and between layers, causing significant deviations during the process evolution. This variation has been mainly attributed to temperature accumulation within the part due to the deposition trajectory and part geometry. Previous works have shown that in certain conditions a self-stabilizing process occurs, maintaining a deposit height and a constant standoff distance between the part and the deposition nozzle. In this work, the link between the powder catchment efficiency and the deposition height stability is illustrated. To this purpose, an experimental system consisting of an online measurement of the specimen weight and a coaxial optical triangulation monitoring of the layer height was employed. Through analytical modeling the inline height measurement and the process parameters could be used for estimating the deposition efficiency in real-time, which was confirmed by the direct mass measurements. The data were used for understanding how the powder catchment efficiency varied and stabilized as the process proceeded in different conditions. The results confirm that the track height variations are caused mainly by powder catchment efficiency, which is governed by the melt pool relative position with respect to the powder cone and the laser beam. For a given set of parameters, the standoff distance can be estimated to achieve the highest powder catchment efficiency and a regular height through the build direction.

Keywords: laser metal deposition; additive manufacturing; process monitoring; deposition efficiency; process stability; optical metrology

1. Introduction

Laser metal deposition (LMD) is an additive manufacturing (AM) process belonging to the directed energy deposition (DED) family [1]. The process employs a laser beam as energy source and powder feedstock, which are conventionally sent to the deposition region in a coaxial manner. The laser beam creates a melt pool to which the powder is blown, generating the deposition tracks. Complex parts can be made by the consecutive deposition of adjacent tracks and layers. LMD is a highly appealing metal AM process due to the capability of producing large parts [2], developing components with variable slicing axis [3], producing parts with multi-material deposition [4], building features on existing components, and the possibility of repairing damaged parts [5]. Despite these several advantages, the LMD process is still not widely applied in an industrial scale. Some of the key issues limiting its industrial application are the limited geometrical stability and the requirement of post-processing [6]. In LMD the deposited track dimensions vary as a function of the process parameters, but can also depend on the deposition trajectory and part geometry. While for instance in laser powder bed fusion (LPBF) the layer height relies on the powder bed lowering, in LMD the deposition track height can vary with the same set of parameters and material due to the thermal history of the process.

In industrial practice, the LMD process parameters are set for achieving mainly pore and crack free deposits [7]. These parameters are then used for generating complex geometries, which can often fail to respect the required geometrical tolerances [8]. Such kind of problem may rise from heat accumulation during the process in acute corners or the decrease of the scanned section area, where the deposit height can increase compared to the nominal one. Inversely, the process may derive to a colder stage with long deposition tracks: in this case, the deposit height can be lower than expected and the part may fail to grow. These effects can be mitigated by choosing the optimal set of process parameters from preliminary experimental campaigns or numerical simulations [9]. While this approach is effective in resolving bigger issues such as part failure, offline optimization can be time-consuming and does not allow the system to autonomously operate: the actual process fluctuations related to the powder-laser interaction remain uncontrolled, leading to unrepeatable results. Indeed, industrial LMD systems can operate with closed-loop controllers, commonly relying on coaxial pyrometers [10], digital cameras [11], or composite systems [12]. These devices aim to maintain a required process temperature and stable deposition conditions. However they require careful calibration methods, which can also be different for bulky to thin structures. Other inline monitoring devices such as optical triangulation [13] or low-coherence interferometry [14] have been also proposed for a direct measurement of the deposit height, which can be compensated by the machine axis movement. Despite several achievements to compensate these changes in the deposited track height, more attention is required for developing a fundamental understanding of the process physics.

The material deposition stability is strictly related to the capacity of the process to maintain the rate of powder being fused. For instance, the LDM process compared to its counterpart that uses wire feedstock, laser metal wire deposition (LMWD), is characterized by higher resolution but lower deposition efficiency [15]. In particular, powder catchment efficiency is a key parameter that defines the amount of material being deposited compared to the amount being released to the deposition area. This relies on the interplay between powder jet, laser beam, and laser process parameters, which determine the deposition track geometry [16]. Powder catchment efficiency has been one of the earliest research questions of LMD [17]. The main importance has been given to the material usage, as the main aim has been to identify the conditions for an environmentally and economically viable process [18]. For more expensive alloys such as Ti- and Ni-alloys, the material cost can become an important fraction of the overall operation costs in LMD based production. Nonetheless, the powder catchment efficiency can be a key element for understanding the deposition stability. Recently a method for the powder flow measurement by a precision scale has been demonstrated and correlated to the actual deposition efficiency measured from single tracks [19]. On the other hand, to the authors' knowledge no previous work attempted to measure the powder catchment efficiency in real time on multiple-track multiple-layer depositions.

The layer height in LMD is known to vary starting from the first deposition stages, since the initial layers are characterized by a certain kind of process instability [20]. This behavior is determined by a layer growth rate variability given by the mismatch between deposition height and part design, which can move

on a stable value during the deposition progress [21, 22]. Such self-regulation mechanism can be related to a change in the powder catchment efficiency during the deposition: this can eventually converge to a stationary regime, although generating transitory geometric inaccuracies [23]. Accordingly, different works faced up to the influence of powder distribution and defocusing on height variability and deposition efficiency while building multi-layer parts [24, 25]. However, an extensive study and modeling regarding the interplay between deposition growth and powder catchment efficiency is still required for a full comprehension of deposition stabilization and optimization. This way, the phenomena behind the geometrical deviations, especially in the deposition height, can be revealed and compensated throughout the process evolution.

This work proposes an innovative approach to study the powder catchment efficiency in LMD of multi-track multi-layer parts in real-time. In particular, the role of deposition height in the mechanism of passive process stabilization was investigated. An analytical model was developed to link the powder catchment efficiency to the deposition height growth and to the main process parameters. An inline experimental setup was developed to measure the mass increase of the deposit during the process. The deposition height was simultaneously measured via a coaxial optical triangulator during the deposition of AISI 316L cubic samples with a three-jet nozzle and a multimode fiber laser. The data obtained from the multiple measurement instruments were used in a complementary way to identify the factors that influence the powder catchment efficiency. The results clearly indicated that self-regulation is associated to the powder catchment efficiency reduction. In the outlook, the proposed model might be used to identify the optimal parameters in terms of both process stability and efficiency, and it can be functional for an active control of the deposition accuracy by means of optical dimensional monitoring.

Nomenclature	
η_m	powder catchment efficiency
η_m^*	effective powder catchment efficiency
η_{path}	deposition path contribution to η_m
η_h	geometrical powder catchment efficiency
η_{th}	theoretical powder catchment efficiency
η_{en}	energetic contribution to η_{th}
η_{int}	powder-laser interaction contribution to η_{th}
m_{dep}	deposited mass
\dot{m}_{dep}	deposition mass rate
\dot{m}_{lost}	powder mass loss rate
\dot{m}_{tot}	total delivered powder mass flow rate
Δt_{dep}	deposition time
Δt_{ON}	interval of laser emission during Δt_{dep}
Δt_{OFF}	interval without laser emission during Δt_{dep}
A_{cs}	single track cross-section area
k_g	single track shape factor
w_t, h_t	single track width and height
h	layer height
h_{th}	theoretical layer height
S	standoff distance
S_0	reference standoff distance
S_{th}	theoretical standoff distance
H	deposited part height
R	deposition head height coordinate
r_x, r_z	robot path transverse and height increments
Δh	height mismatch between h and r_z
N_t	track number for each layer
N_l	total layer number
v	transverse scanning speed
P	processing laser power
P_0	saturation power for powder melting
ρ	solid material density
C_p	solid material specific heat capacity
L	material fusion latent heat
\mathcal{A}	material optical absorptance
T_m	material melting point
T_0	room temperature
ΔT	temperature increase during powder deposition
A_p, A_l	powder and laser beam spot areas
A_{int}	interaction area between laser and powder beams
d_{p0}	powder delivery channel diameter at nozzle tip
x_{p0}	radial distance of powder channel orifices
x_{p1}, z_{p1}	extrapolated powder cone apex coordinates
α_p	single powder jet half-divergence
β_p	single powder delivery channel inclination angle
a_{p1}, a_{p2}	elliptical axes of single powder jet transverse section
x_p, x_l	powder and laser spot border coordinates
c_g	geometrical correction factor to x_l
w_{l0}	laser beam waist radius
θ_l	laser beam half-divergence
z_{l0}	laser focus axial coordinate

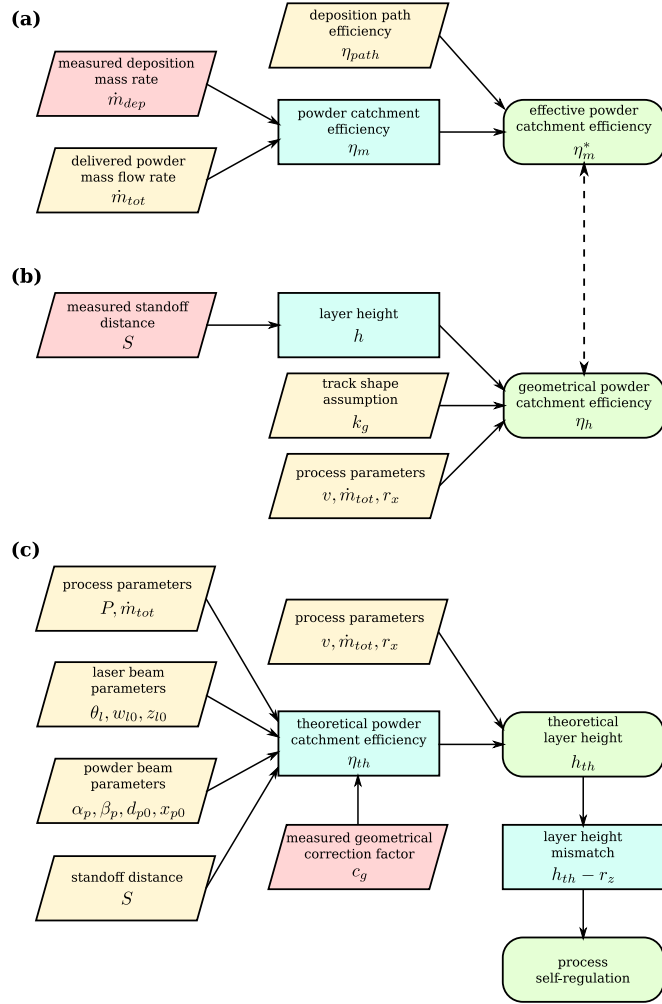


Figure 1: Main steps of the powder catchment efficiency models presented in the text.

2. Model

In the following sections the deposition efficiency will be treated from different point of views. Section 2.1 provides a general definition of the powder catchment efficiency, which can be applied to direct measurements of the deposition mass, as summarized in Figure 1(a). In section 2.2 a layer height model provides an alternative solution to define the powder catchment efficiency in terms of geometrical considerations, which can be applied to deposition height measurements in bulk depositions, as represented in Figure 1(b). The equivalence of these different efficiency definitions will be demonstrated in the experimental part of this work by means of independent measurements. Finally, section 2.3 presents a semi-empirical model for the interpretation of the deposition process stability, where the powder catchment efficiency is expressed as a function of process parameters and standoff distance; the main steps of the model are summarized in Figure 1(c). In particular, the presented model links the process self-stabilization mechanisms observed in the deposition height growth to the powder catchment efficiency variability, which is determined by the variable interaction between powder and laser beams.

2.1. Definition of powder catchment efficiency

The instantaneous powder catchment efficiency η_m is defined as the ratio between the deposition mass rate \dot{m}_{dep} , i.e. the increase of the deposit mass in a given time interval, and the total mass flow rate \dot{m}_{tot} of the metallic powder which gets delivered during the deposition, including the powder loss rate \dot{m}_{lost} :

$$\eta_m = \frac{\dot{m}_{dep}}{\dot{m}_{tot}} = \frac{\dot{m}_{dep}}{\dot{m}_{dep} + \dot{m}_{lost}}. \quad (1)$$

Hereafter the total powder flow rate $\dot{m}_{tot} = \dot{m}_{dep} + \dot{m}_{lost}$ is assumed as a known process parameter, constant in time.

A direct experimental estimation of η_m can be obtained by measuring the mass Δm_{dep} deposited during a finite time interval Δt_{dep} , e.g. the interval for the deposition of a multi-track layer. The average efficiency over the corresponding interval is therefore

$$\bar{\eta}_m = \frac{\Delta \bar{m}_{dep}}{\Delta t_{dep} \dot{m}_{tot}}. \quad (2)$$

However, it must be considered that the deposition procedure for a non-trivial geometry can include intervals where the laser emission is not enabled. For example this may be required during the robot position settlement between different tracks or layers. Conversely, the powder feed is typically kept constant in order to maintain a stationary flow, considering the slow response time of common powder deliver systems. Of course the powder which gets delivered when the processing laser is disabled cannot be deposited and gets lost. Indeed the average powder catchment efficiency defined in Eq. (2) includes an implicit factor η_{path} that is not related to the process itself, but which is set by the chosen deposition path strategy. This can be expressed as the ratio between the time of processing laser emission Δt_{ON} over the total deposition time interval Δt_{dep} :

$$\bar{\eta}_{path} = \frac{\Delta t_{ON}}{\Delta t_{dep}} = \frac{\Delta t_{ON}}{\Delta t_{ON} + \Delta t_{OFF}}. \quad (3)$$

Therefore, in real-world measurements, the average efficiency $\bar{\eta}_m$ must be normalized to $\bar{\eta}_{path}$ to eliminate the dependence on the specific deposition strategy, hence introducing the effective efficiency $\bar{\eta}_m^*$ related only to the deposition process physics and defined as

$$\bar{\eta}_m^* = \frac{\bar{\eta}_m}{\bar{\eta}_{path}}. \quad (4)$$

2.2. Calculation of efficiency from deposition layer height

The powder catchment efficiency definition can be obtained also from geometrical considerations. Assuming the absence of porosity, the mass deposition rate is related to the cross-section area A_{cs} of a single deposition track as

$$\dot{m}_{dep} = A_{cs} v \rho \quad (5)$$

with v being the transverse scanning speed and ρ the bulk material density. Referring to Figure 2(a), the cross-section area of a generic deposition track can be expressed as

$$A_{cs} = k_g w_t h_t \quad (6)$$

where h_t and w_t are the track height and width, while k_g is a geometrical factor which depends on the track shape. E.g., in case of a half-elliptical track $k_g = \frac{\pi}{4}$, while for a rectangular track $k_g = 1$. Therefore the powder catchment efficiency can be calculated from the track geometry by inserting Eq. (5) into the general definition of Eq. (1):

$$\eta_h = \frac{k_g w_t h_t v \rho}{\dot{m}_{tot}}. \quad (7)$$

Considering the deposition of a simple prismatic geometry composed of multiple tracks and multiple layers, referred to as bulk deposition from hereon, each layer is composed of N_t adjacent tracks separated by

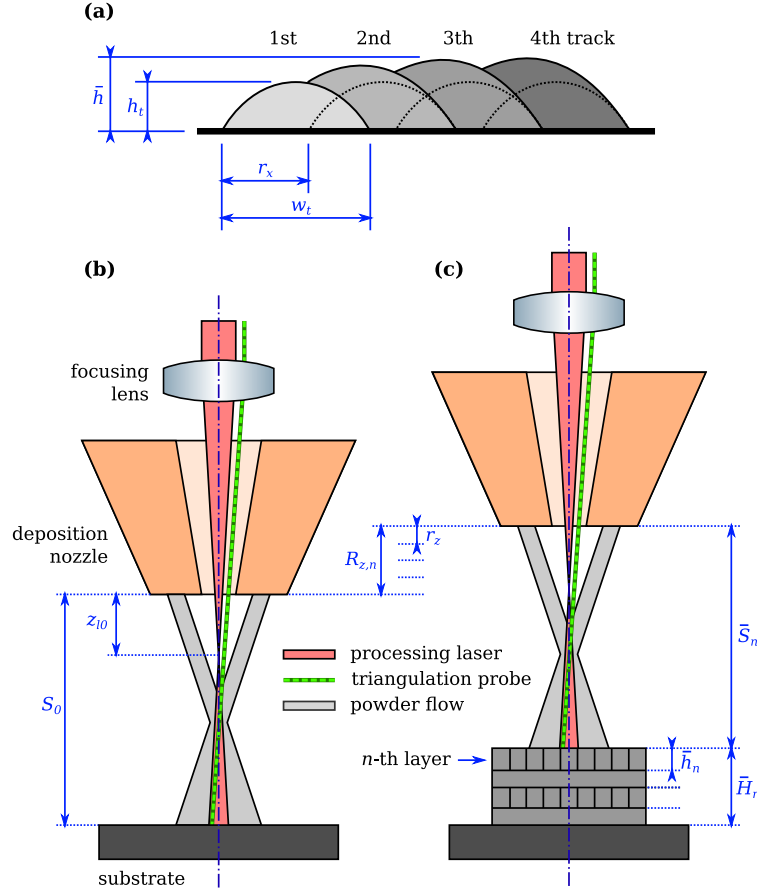


Figure 2: (a) Qualitative cross-section representing the characteristic dimensions for a deposition with partially overlapping tracks, seen along the scanning direction: h_t and w_t are the single track height and width, r_x is the path transverse increment, \bar{h} is the average layer height reached after an initial transient; dashed lines represent the single tracks spaced by r_x expected in absence of overlapping effects. (b-c) Qualitative section representing the characteristic dimensions related to deposition height during a multi-layer deposition by means of a robotized head following an alternating scanning direction, with the laser and powder beams delivered through a nozzle: (b) initial condition, (c) after n layers.

a path transverse increment or pitch r_x , which is assumed constant in the current discussion. A minimum requirement for a bulk deposition without empty volumes is that the single track width must exceed the path transverse increment, thus $w_t > r_x$. This is a necessary condition for a partial overlap between each newly deposited track and the previous one within the same layer. Therefore r_x is a relevant parameter for the determination of the bulk cross-section area A_{cs} , since it influences the effective track width and height. This can be understood considering that, in the presence of track overlapping, the incident laser beam partially remelts the material which was already deposited, while the incoming powder flow contributes to the height growth over the whole deposition region, hence also over the previous track. Indeed track overlapping translates in an actual height growth excess: inclined tracks are typically observed in multi-track LMD [26]. Different geometrical models can be proposed to predict such track overlap effects [27], which are intrinsically linked with the mechanisms of melt pool formation [28]. In general, the experimental evidence is characterized by an initial transient in the track shape, which converges rapidly to a stationary regime within few adjacent tracks for a sufficiently high overlapping factor, defined as $0 < (w_t - r_x)/w_t < 1$.

From purely geometrical considerations and in the simplified assumption of a stationary process, i.e. with the track width w_t and height h_t not varying significantly within the same layer, the average contribution given by each track to the layer deposition is equivalent to a rectangular cross-section whose dimensions are set by the path transverse increment r_x and by the average layer height \bar{h} . Therefore, under the previous hypotheses, $k_g = 1$ and the cross-section area of Eq. (6) averaged over a multi-track layer becomes

$$\bar{A}_{cs} \simeq r_x \bar{h}. \quad (8)$$

The error introduced by such approximation is of the order of $w_t h / N_t$, whose contribution is negligible if the number of tracks which compose the layer is sufficiently big. This is a realistic condition for bulk depositions with $N_t \gg 1$.

The powder catchment efficiency defined in Eq. (7) in terms of geometrical parameters can be averaged over a multi-track layer interval and labeled as $\bar{\eta}_h$. The results for the average cross-section area of Eq. (8) can be applied. It follows that, if the deposition parameters r_x , \dot{m}_{tot} and v are fixed and if the deposition process is stationary within each layer, $\bar{\eta}_h$ depends only on the average layer height \bar{h} :

$$\bar{\eta}_h \simeq \bar{h} \frac{r_x v \rho}{\dot{m}_{tot}}. \quad (9)$$

It is important to highlight that the definition of $\bar{\eta}_h$ is equivalent to the one of $\bar{\eta}_m^*$ given in Eq. (4): $\bar{\eta}_h$ and $\bar{\eta}_m^*$ provide different ways to estimate the average powder catchment efficiency, respectively from height and weight measurements. The validity of the hypotheses and approximations introduced in the model will be investigated in the experimental study by comparing the two expressions.

Eq. (9) shows that the geometry-related efficiency $\bar{\eta}_h$ in bulk depositions is determined by the deposition layer height, hence the study of powder catchment efficiency can be indirectly performed by means of dimensional measurements. Specifically, considering a LMD system based on a robotized deposition head, \bar{h} can be extracted using a displacement sensor which measures the standoff distance \bar{S} , defined as the distance between the deposition nozzle tip and the deposition surface. Considering a multi-track multi-layer deposition, and referring to Figure 2(b-c), the average standoff distance \bar{S}_n for the n -th layer can be expressed as

$$\bar{S}_n = S_0 + R_{z,n} - \bar{H}_n \quad (10)$$

where S_0 is the initial standoff distance value, $R_{z,n}$ is the relative robot height coordinate after n layers, and \bar{H}_n is the deposited structure height averaged within the considered layer. Consequently during the evolution of the deposition process the standoff distance can drift from its initial value due to instabilities in the deposition height, i.e. when $R_{z,n} \neq \bar{H}_n$.

The deposit height \bar{H}_n at layer n is the sum of the layer height \bar{h}_i for all the previous layers $i = 1 \dots n$, thus

$$\bar{H}_n = \sum_{i=1}^n \bar{h}_i. \quad (11)$$

Analogously, the robot height coordinate R_n at layer n is the sum of the robot height increment $r_{z,i}$ for i ranging from 1 to n . Here $r_{z,i} = r_z$ is considered a constant parameter during the whole deposition, thus

$$R_{z,n} = \sum_{i=1}^n r_{z,i} = nr_z. \quad (12)$$

Therefore the n -th layer height can be calculated from standoff distance differentiation as

$$\bar{h}_n = \bar{H}_n - \bar{H}_{n-1} = r_z + \bar{S}_{n-1} - \bar{S}_n. \quad (13)$$

This shows explicitly that the standoff distance \bar{S} remains constant only if the layer height \bar{h} matches the robot height increment r_z .

2.3. Model for efficiency and height self-regulation

In an open-loop approach the robot height increment r_z is kept fixed during a multi-layer deposition. For an ideal process growth such increment of the deposition head height should match the deposited layer height h . However this condition is unlikely satisfied in real-world cases: a height mismatch $\Delta h = h - r_z \neq 0$ is typically present if the process parameters are not carefully modeled or actively controlled. Moreover Δh can change during the deposition due to the intrinsic process efficiency variability. From Eq. (13) a positive height mismatch $\Delta h > 0$ corresponds to a growth which is faster than the robot movement along the build direction, and leads to a lower standoff distance; on the contrary, a negative mismatch $\Delta h < 0$ leads to a greater standoff distance, hence to a departure of the deposition area from its initial relative position.

A monotone mismatch $\Delta h \neq 0$ would cause a standoff distance divergence, eventually ending with a failure of the process itself when the deposition surface becomes too far or too close relatively to its optimal distance. However, when the laser and powder beams are focused along the axial direction, changes in the standoff distance S are also associated to variations in the process conditions related to laser intensity and powder flux on the deposition area [22]. In particular, the presence of a non-zero gradient of Δh with S can lead to a stationary regime where $\Delta h = 0$. This corresponds to a transient which brings the process growth to match the robot movements, hence to maintain a steady standoff distance [23]. Inline optical monitoring can be exploited for a direct observation of the process evolution and stabilization during the deposition of complex parts [20]. In general, this mechanism is favorable because it reflects a passive process robustness against perturbations, and because it corresponds to an enhanced geometrical accuracy since the actual deposition process matches the design model in the stationary regime.

The relation between deposition self-regulation and efficiency must be investigated in terms of energy and powder transverse distributions [19]. The current work considers the case study configuration where the focal points of the laser and powder beams lay between the powder nozzle tip and the initial substrate position. In this common condition the open-loop self-stabilizing regime can be observed after a transient to smaller standoff distance values, i.e. with positive layer mismatch $h > r_z$. Such faster growth can be interpreted as the result of an increasing substrate temperature that favors powder melting at the beginning, in combination with a powder flux abundance which allows to deposit layers with high efficiency. Typically substrate temperature stabilization occurs after few layers [26], thus the effects of energy and powder spatial distributions dominate on the subsequent deposition growth rate. Moreover, the initial values of standoff distance and layer height increment play an important role in the dynamics of process stabilization [24]. It follows that the powder flux fraction available for catchment into the melt pool generated by the laser radiation changes while approaching the powder nozzle tip. This can introduce a powder catchment efficiency reduction, corresponding to a braking-like effect for the deposition growth, as a natural feedback mechanism which leads to a stationary regime where $h = r_z$.

Several approaches can be followed for modeling the deposition height in terms of the laser-powder interaction, based on either analytical [29], numerical [30], or dimensional [31] descriptions. Here a semi-empirical model is proposed for a quantitative interpretation of process self-regulation for bulk geometries, extending the results reported in other works [32]. Specifically, the theoretical powder catchment efficiency η_{th} is derived with an explicit dependence on the standoff distance S and on the process parameters, assuming

a stationary deposition. In particular η_{th} is defined as the product of two terms, one related to energetic factors η_{en} , the other depending on the powder-laser spatial interaction η_{int} for a specific deposition nozzle configuration:

$$\eta_{th} = \eta_{en} \eta_{int}. \quad (14)$$

Some assumptions have to be introduced for the calculation of η_{int} . First of all, the laser-powder interaction is assumed to happen only within the area A_{int} corresponding to the intersection between the respective beams on the deposition surface. This determines the effective powder mass rate which can be captured in the melt pool generated by the laser radiation. Secondly, the approximation of uniform powder mass flux and laser intensity over the respective spot areas A_p and A_l is introduced for simplicity. Therefore

$$\eta_{int} = \frac{A_{int}}{A_p}. \quad (15)$$

From an energetic point of view, powder efficiency saturation is typically observed while increasing the laser power, which can be attributed to the substrate dilution phenomenon [33, 34]. Accordingly, here η_{en} is modeled as the powder fraction which can be melt by the laser power P , normalizing P to the power P_0 that is required to fuse the total powder flow rate \dot{m}_{tot} . Such saturation power can be derived from the lumped heat capacity model [35] as

$$P_0 = \dot{m}_{tot} \frac{C_p \Delta T + L}{\mathcal{A}}, \quad (16)$$

where C_p is the material specific heat, $\Delta T = T_m - T_0$ is the excursion between room temperature T_0 and melt pool temperature T_m , L is the fusion latent heat, and \mathcal{A} is the material optical absorptance. In usual conditions T_m can be roughly approximated with the material melting point, as assumed here. Finally, a gaussian sigmoid function can be used to express in a simplified way the energetic efficiency term η_{en} [36]. This allows to smoothly connect η_{en} in the linear scaling regime for $P \ll P_0$ with the saturating trend when $P \rightarrow P_0$, while tending asymptotically to 1 for $P \gg P_0$:

$$\eta_{en} = 1 - \exp\left(-\frac{P}{P_0}\right). \quad (17)$$

It follows that the semi-empirical relation for the theoretical powder catchment efficiency becomes

$$\eta_{th} = \frac{A_{int}}{A_p} \left[1 - \exp\left(-\frac{P\mathcal{A}}{\dot{m}_{tot}(C_p \Delta T + L)}\right) \right]. \quad (18)$$

An approximated geometrical model for the powder distribution can be provided for the calculation of A_{int} and A_p , based on simple geometrical considerations. Similar methods have been reported for the description of different configurations [37]. Here a three-jet nozzle is considered, composed of 3 tilted powder streams arranged with axial symmetry at 120° . These form a hollow cone-like powder stream, coaxial to a focused laser beam passing along the nozzle axis. Each of the 3 powder jets can be seen as a cone having divergence angle $2\alpha_p$ outgoing from the nozzle tip as shown in Figure 3, with the cone axis tilted by β_p relatively to the transverse plane. The diameter d_{p0} of the powder delivery channel at the nozzle tip exit is assumed as a constrain for the powder cone basis at $S = 0$, whose center lays at distance x_{p0} from the origin placed in the nozzle tip center. Since β_p , d_{p0} and x_{p0} are known from the nozzle geometry, while α_p can be determined experimentally by observing the powder flow with a camera, the coordinates of the hypothetical powder cone apex relatively to the nozzle tip center can be extrapolated as

$$\begin{aligned} x_{p1} &= -\frac{d_{p0}}{2} \frac{\cos \beta_p}{\tan \alpha_p} - x_{p0} \\ z_{p1} &= \frac{d_{p0}}{2} \frac{\sin \beta_p}{\tan \alpha_p}. \end{aligned} \quad (19)$$

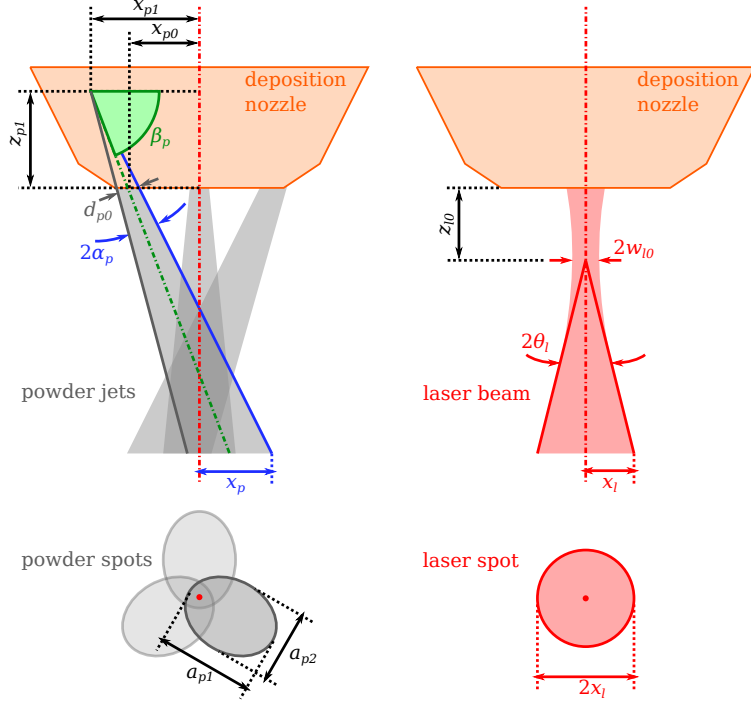


Figure 3: Qualitative side view of the powder nozzle, highlighting the main dimensions related to the 3 conical powder jets ejected from the respective nozzle tip orifices (left) and to the laser beam (right). The corresponding powder and laser beam spots in the transverse plane are represented in the bottom.

Under the previous assumptions and referring to Figure 3, it can be demonstrated that the major axis of the elliptical transverse section for each powder cone at a generic standoff distance $S > 0$ is

$$a_{p1} = (S + z_{p1}) \left(\frac{1}{\tan(\beta_p - \alpha_p)} - \frac{1}{\tan(\beta_p + \alpha_p)} \right). \quad (20)$$

The corresponding minor axis is

$$a_{p2} = 2(S + z_{p1}) \frac{\tan \alpha_p}{\sin \beta_0}. \quad (21)$$

Accordingly, the effective total area for the 3 elliptical powder sections is

$$A_p = \frac{3\pi}{4} a_{p1} a_{p2}. \quad (22)$$

The following regimes can be identified for the calculation of the interaction area A_{int} depending on the standoff distance, referring to Figure 4.

- Closer than a minimum standoff distance value there is no intersection between laser and powder spots, thus $A_{int} = 0$ and the melt pool does not intercept the metallic powder flux.
- Above a characteristic standoff distance the laser spot fully overlaps with the powder area. If the powder spot diameter is bigger than the laser spot diameter the interaction area is limited by the laser beam, hence $A_{int} = A_l$. This means that in principle the powder can be caught over the whole melt pool area. The initial standoff distance S_0 is typically chosen in this regime for precision depositions where a good transverse resolution is required.
- In the intermediate region there is a strong dependence of A_{int} on S , since only part of the melt pool area can intercept the powder flux. In a first approximation the interaction area can be calculated as

the sum of 3 circular segments, as represented in Figure 4(c). This assumption is valid if the laser spot diameter is significantly smaller than the elliptical axes a_{p1} and a_{p2} of the powder cone sections. Such condition is verified in the typical working range of S for the system configuration considered here.

- Above a certain standoff distance value another zone of partial intersection is present, tending to $A_{int} = 0$. However this case is neglected in the current model since it lays far from the common working conditions, and because it corresponds to an unstable deposition regime.

The coordinates for the powder and laser spot borders relatively to the nozzle axis are represented in Figure 4(a), calculated for the nozzle configuration of the current experimental study. These are defined as

$$\begin{aligned} x_p &= \frac{S + z_{p1}}{\tan(\beta_p - \alpha_p)} + x_{p1} \\ x_l &= c_g \sqrt{w_{l0}^2 + \theta_l^2 (S - z_{l0})^2} \end{aligned} \quad (23)$$

and referred to the nozzle tip center. In particular, x_p represents the inner cone border of the powder jet. The laser spot limit x_l is assumed as the gaussian beam radius, and it can be calculated at the standoff distance S knowing the $1/e^2$ beam waist radius w_{l0} , the beam half-divergence θ_l , and the focus position z_{l0} along the beam axis relative to the nozzle tip. A dimensionless geometrical factor c_g is included in x_l : it summarizes the effects of the approximations introduced in the geometrical model, and in particular the discrepancy between laser spot and the actual melt pool size. This parameter will be determined *a posteriori* by fitting the model predictions to the experimental results, finding a value close to 2. It must be noted that c_g can be influenced by thermal accumulation effects, depending on the chosen deposition strategy. Such empirical calibration approach is convenient due to the complexity of a comprehensive quantitative modeling for the actual interaction between laser and powder beams.

The laser-powder interaction area is calculated from x_p and x_l considering the effect of superimposition for the 3 powder jets:

$$\begin{aligned} x_p \leq -x_l &: A_{int} = 0 \\ -x_l < x_p < x_l &: A_{int} = 3 \left(x_l^2 \arccos \left(\frac{-x_p}{x_l} \right) + x_p \sqrt{x_l^2 - x_p^2} \right) \\ x_p \geq x_l &: A_{int} = 3\pi x_l^2 \end{aligned} \quad (24)$$

In the approximation of uniform powder and laser energy distributions within the respective spot areas, $\eta_{int} = A_{int}/A_p$ can be taken as the fraction of powder flow which can interact with laser beam, hence which can contribute to the effective melt pool and layer growth. This ratio can be calculated from Equations (22) and (24), and it depends on the standoff distance as plotted in Figure 4(b). Accordingly the theoretical powder catchment efficiency η_{th} can be determined analytically as a function of S for every process condition for a specific nozzle geometry.

From a different point of view, the theoretical layer height can be calculated from η_{th} as a function of standoff distance exploiting Eq. (9):

$$h_{th} = \eta_{th} \frac{\dot{m}_{tot}}{r_x v \rho} \quad (25)$$

This allows to simulate the standoff distance at layer n as

$$S_{th,n} = S_0 + \sum_{i=1}^n (h_{th,i} - r_z) \quad (26)$$

considering the initial standoff distance S_0 , and with the i -th layer height $h_{th,i}$ being calculated at $S_{th,i-1}$. It can be observed that self-regulation can happen when the gradient $\partial h_{th}/\partial S$ is greater than zero and $h_{th,0} > r_z$, necessary conditions to reach the $h_{th} = r_z$ matching. The proposed method can represent an interesting tool for the prediction of the deposition growth for a given set of process parameters, allowing for an analytical study of the self-stabilization mechanisms, as well as for the offline efficiency optimization and geometrical accuracy control.

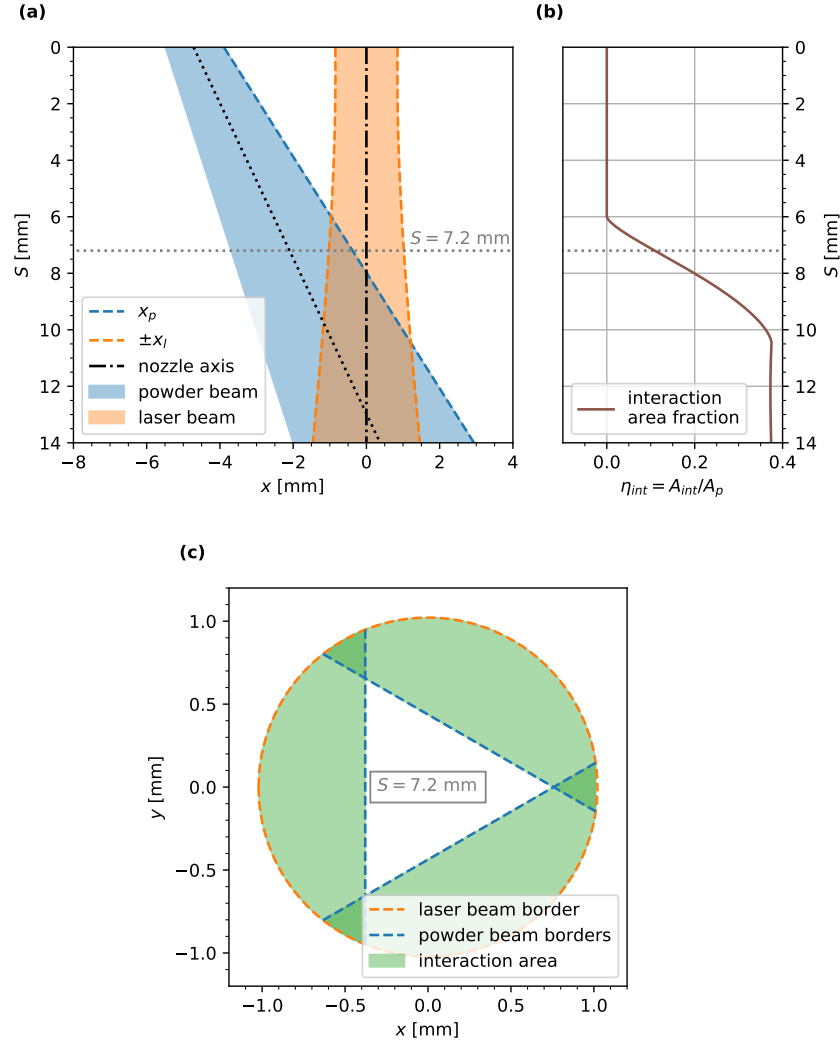


Figure 4: (a) Quantitative representation of the coaxial laser beam and one of the 3 powder beams along the axial direction; the origin is placed at the nozzle tip in $S = 0$. (b) Laser-powder interaction area fraction η_{int} (horizontal axis) calculated as a function of standoff distance S (vertical axis). (c) Transverse section of the laser and powder beams, taken at the example standoff distance represented by the dashed gray line; the regions shaded in green represent the approximated laser-powder interaction area. A geometrical correction factor $c_g = 2.19$ has been considered for x_l . The laser and powder beam geometry reflect the experimental configuration considered in the current study.

Table 1: Chemical composition of the employed AISI 316L powder.

Element	Fe	C	Si	Mn	P	S	Cr	Mo	Ni
Weight % (base)		0.023	0.36	1.30	0.016	0.005	16.96	2.45	10.89

Table 2: Physical properties of solid AISI 316L stainless steel [21].

Property	Value
density ρ	$8 \times 10^3 \text{ kg/m}^3$
melting temperature T_m	1670 K
specific heat C_p	500 J/(kg K)
fusion latent heat L	300 kJ/kg
optical absorptance \mathcal{A}	0.35

3. Materials and methods

3.1. LMD system

The LMD system is equipped with a fiber laser (IPG Photonics YLS 3000), having 1070 nm emission wavelength and 3 kW maximum power. The radiation is delivered by a 50 μm feeding fiber, coupled with a 400 μm process fiber by a fiber-to-fiber coupler. The LMD setup comprises a deposition head (Kuka Industries MWO-I-Powder), equipped with a 129 mm focal length lens to collimate the laser beam, and with a 200 mm focal length lens to focus it on the working area. The collimation is adjusted in order to have a 1.2 mm laser spot diameter at the reference standoff distance $S_0 = 12 \text{ mm}$. An optical monitoring setup can be integrated to the deposition head exploiting a dichroic mirror, as described in the following sections.

The deposition head includes a three-jet nozzle (Fraunhofer ILT 3-JET-SO16-S) for powder delivery. The powder flow is controlled by a powder feeder (GTV TWIN PF 2/2-MF). Argon is used as carrier gas to deliver the powder from the feeder up to the three-jet nozzle. During the process argon is used also as shielding gas. The deposition head is mounted on a 6-axis anthropomorphic robot (ABB IRB 4600-45).

3.2. Powder and substrate materials

The employed powder is AISI 316L stainless steel, produced by Carpenter Additive. The powder chemical composition is reported in Table 1. The physical properties of bulk AISI 316L are reported in Table 2. The powder is characterized by a spherical shape, with a particle diameter in the range of 45 – 90 μm . The powder was deposited on AISI 316L substrates having 10 mm thickness and $22 \times 22 \text{ mm}^2$ dimensions.

3.3. Laser and powder beam characteristics

The focused processing laser beam was characterized using a beam analyzer (PRIMES FocusMonitor). The measured laser beam parameters are reported in Table 3. The focus position z_{l0} was referred along the laser head axis, with the origin set at the powder nozzle exit.

In Section 2.3 the powder distribution has been modeled in terms of the three-jet nozzle geometry, with each of the 3 powder jets contributing to form a common beam that hits the deposition region, coaxially to the laser beam. The powder beam parameters measured for the 3-JET-SO16-S nozzle are

Table 3: Characteristics of the processing laser beam.

Property	Value
waist diameter $2w_{l0}$	0.77 mm
divergence $2\theta_l$	83 mrad
focus position z_{l0}	0.9 mm

Table 4: Characteristics of each single powder jet contributing to the powder beam, referring to Figure 3.

Property	Value
powder jet half-dispersion α_p	6°
delivery channel inclination β_p	70°
delivery channel orifice diameter d_{p0}	1.5 mm
delivery channel orifice radial position x_{p0}	4.7 mm

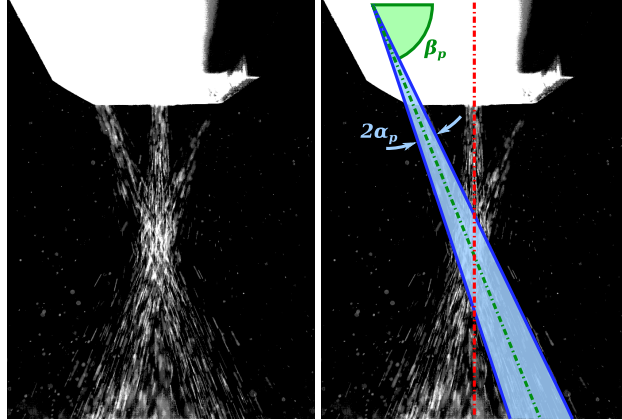


Figure 5: Image of the 3 powder jets spreading from the deposition nozzle, acquired using a camera in combination with external illumination. The characteristic angles for a single powder cone are highlighted on the right.

reported in Table 4. The delivery channel inclination β_p , orifice diameter d_{p0} , and orifice radial position x_{p0} were extracted from the nozzle geometrical model, defined relatively to the nozzle tip as represented in Figure 3. The dispersion angle of the single powder jet was determined experimentally by means of offline characterization, in absence of the processing laser emission. Indeed, the powder flow was acquired using a high-speed CMOS camera (Photron Fastcam Mini AX200) at 1 ms shutter time, considering the same conditions used for the experiments in terms of mass flow rate, carrier gas flow, and shielding gas flow. External illumination was used to highlight the trajectories of the powder particles, using a high-power white LED lamp. An example of image is reported in Figure 5. The dispersion $2\alpha_p$ was estimated as the angle which contained the 98 % of the powder particles for a single jet.

3.4. System for real-time deposition mass measurement

The novel system used for the real-time measurement of the deposition mass is sketched in Figure 6. The device was designed for independent measurements of the deposited and lost powder masses as a function of time during the deposition process. Such measurements were performed with two load cells based on strain gauges, that transduce the mechanical deformation induced by masses into a variation of electrical resistance. Each load cell included four strain gauges connected in a Wheatstone bridge configuration, insensitive to the distance of force application along the cell bar. The strain gauge bridge signal was amplified with an instrumentation amplifier circuit (Texas Instruments INA125P).

The first load cell was directly connected to the deposition substrate to measure the powder mass which was deposited. The dimension of the substrate was fitted to the programmed deposition path, allowing the unmelted powder to fall without accumulating on the substrate itself. The second load cell sustained a hopper to measure such lost powder. The hopper was used also as a protection system to avoid accumulation of powder around the measurement device. The hopper was made of brass sheet with 0.9 mm thickness. The choice of the material was related to the high heat dissipation of brass, which was important due to the high temperatures reached around the process region. The hopper implemented a self-balancing tip system, centered in the center of mass of a vessel which collected the unmelted powder. The structure was

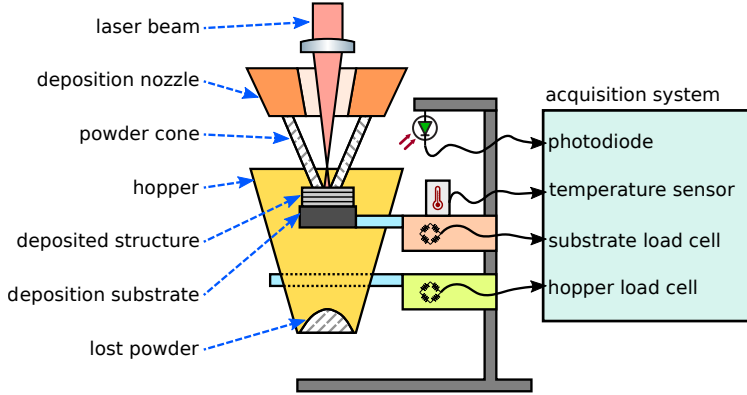


Figure 6: Scheme of the experimental setup for the real-time measurement of the deposited powder mass.

also equipped with an anti-rotation system, consisting in an aluminum bar with two adjustable screws, that ensured greater stability during the deposition process by blocking excessive rotations of the brass vessel.

The entire load cell system was protected from the metallic powder and vapors by a plastic box, to avoid contamination and damaging of the electronic circuits. The box was purged by a continuous flow of argon, assuring gas recirculation and thermal stability. A photodiode was placed close to the deposition region to get a reference signal for the synchronization of the mass measurement with the process laser emission, the robot movements, and the height monitoring.

Thermal insulation has been treated carefully in the setup design. Indeed, the load cells can operate in a limited temperature range, up to 50 °C, and their readout can be strongly influenced by temperature variations. For this reason the load cells were placed far from the process region to avoid thermal damaging. The load cells were connected to the deposition substrate and to the powder hopper by insulating glass bars to suppress thermal conduction. Moreover, the measurement setup and electronics were protected from thermal irradiation using aluminum foils.

The voltage signals from the load cells, the temperature sensor, and the photodiode were acquired at 10 Hz using an acquisition board (National Instruments USB-6009) connected to a computer running a LabVIEW program. The readout voltages of the load cells were calibrated using a set of standard masses, finding a proportionality factor of 0.086 V/g for the substrate cell, and of 0.0191 V/g for the hopper cell, on a scale ranging between 0 V and 10 V.

Possible thermal effects which might perturb the acquisitions were monitored using an analog temperature sensor placed close to the load cell. In fact a temperature dependence was observed above 30 °C while calibrating the load cell. However, thanks to the thermal shielding implemented in the setup, the temperature remained almost stable even in presence of the high-power processing laser radiation during long depositions, with an average temperature of (28.0 ± 1.1) °C over the whole experimental campaign. This allowed to neglect the influence of ambient temperature on the mass measurements.

3.5. Deposition height monitoring with coaxial triangulation

The standoff distance was monitored in real-time during the deposition process using a custom coaxial triangulation setup. A detailed description of the measurement working principle was reported in a previous work [20]. The optical scheme follows the former implementation, with some enhancements described here. A 532 nm 4.5 mW probe laser is integrated in the deposition head optical chain, accessible through a lateral monitoring port. The collimated probe beam is deflected along the deposition optical axis by a dichroic mirror, transparent for the high-power laser wavelength, partially reflective in the visible and near-infrared (NIR) spectrum. The probe beam propagates to the 200 mm focal length lens of the deposition head in a slightly off-axis configuration, hence it gets focused with a non-zero deflection while exiting from the deposition nozzle orifice, as represented in Figure 2(b-c). This introduces a dependence of the transverse probe spot position on the standoff distance. The probe alignment offset of few mm relatively to the lens axis

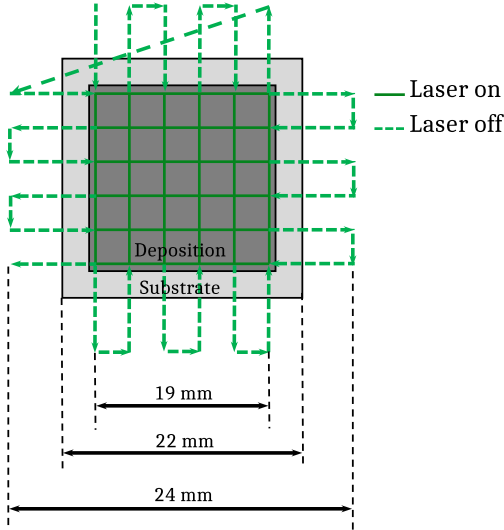


Figure 7: Deposition path strategy for building the square cuboids: each layer is build with an alternated scanning direction, with orthogonal directions for adjacent layers and with the laser emission being enabled only for the intervals required for the actual part deposition.

is chosen in order to get a small deflection angle, keeping the probe spot within the melt pool considering the typical standoff distance variations during the deposition process.

The probe radiation which gets scattered from the melt pool surface is collected by the focusing lens, and back-deflected toward the monitoring port by the deposition head dichroic mirror. The beam crosses a further dichroic shortpass mirror with 650 nm cutoff, used for monitoring techniques in the NIR spectrum such as pyrometry or melt pool imaging, not considered in the current work. Half of the scattered probe radiation is deflected by a 50:50 beam splitter cube towards an iris used for spatial filtering. A 532 nm bandpass filter is used to eliminate spurious radiation. A compact Galilean-like telescope configuration is obtained by combining a 100 mm plano-convex lens with a -25 mm bi-concave lens. Finally the probe spot is imaged on a 1.3 MP CMOS camera having 4.8 μm pixel size (Ximea XiQ MQ013MG-ON).

The probe spot position has been calibrated as a function of known standoff distances [38], finding an enhanced sensitivity factor of 0.106 mm/pixel over a 20 mm standoff distance range. The camera was triggered for the acquisition at 400 fps frame rate, cropping the sensor to a 420×96 pixel area. The shutter time was limited to 1 ms, thanks to the enhanced light collection guaranteed by the 1" clear aperture of the new monitoring optical chain. The images were acquired by means of USB3 interface using a dedicated computer. The standoff distance was extracted in real-time using a Python algorithm: the images were integrated along the short image axis, obtaining a 1D vector; then the probe spot position and size were extracted as the vector distribution moments; finally the standoff distance was calculated applying the calibration curve, and stored for post-processing.

The same program of the triangulation measurement was used to acquire the service variables of the robot system via an ethernet socket connection at a rate of about 100 Hz. These were used to correlate the standoff distance data sets with the deposition head coordinates and with the laser emission.

4. Experimental campaign and sample analysis

The main target of the experimental campaign was the investigation of the link between powder catchment efficiency and height growth in bulk geometries. Square cuboids having $19 \times 19 \times 10$ mm³ nominal dimensions were produced for the scope, obtained by means of multi-layer multi-track deposition. An alternated bi-directional deposition strategy was adopted, following the deposition path sketched in Figure 7.

Table 5: Varied and fixed parameters of experimental campaign.

Varied parameter	Level			[W]
	Low	Mid	Hi	
laser power P	525	612	700	[W]
scanning speed v	22	32	42	[mm/s]
powder feed rate \dot{m}_{tot}	0.11	0.16	0.22	[g/s]

Fixed parameter	Value
robot transverse increment r_x	0.45 mm
robot height increment r_z	0.2 mm
layer number N_l	50
track number N_t (for each layer)	42
initial standoff distance S_0	12.0 mm
initial laser spot diameter (at S_0)	1.2 mm
carrier gas flow rate	7.5 L/min
shielding gas flow rate	25.0 L/min

Table 6: Labels of the considered process conditions.

Label	P [W]	\dot{m}_{tot} [g/s]	v [mm/s]
C1	612	0.16	32
C2	700	0.22	22
C3	700	0.22	42
C4	700	0.11	22
C5	700	0.11	42
C6	525	0.22	22
C7	525	0.22	42
C8	525	0.11	22
C9	525	0.11	42

The experimental campaign followed a 2-level factorial plan for 3 varied parameters plus a central point, corresponding to a total of 9 combinations. The varied parameters were the laser power P , the scanning speed v , and the delivered powder flow rate \dot{m}_{tot} . The central point was chosen as a typical working condition, optimized for bulk depositions with good dimensional resolution, yet representing a compromise for a reduced powder catchment efficiency. The parameters were varied within the typical range suitable to obtain a regular deposition growth. A number of 3 replicates was performed for each deposition condition, for a total of 27 randomized specimens. The fixed and varied parameters of the campaign are reported in Table 5. Each combination of parameters is identified by a progressive label as reported in Table 6.

During the deposition the powder flow was kept continuous due to the slow dynamics of the powder feeder between the turning on and off stages. On the contrary, the laser operation was intermittent, with the emission enabled only for the intervals over the deposition substrate. The intervals with the laser turned off were necessary to avoid transitory effects related to acceleration and deceleration of the robot, even if they introduce an unavoidable inefficiency contribute. The robot transverse increment r_x was chosen to guarantee sufficient overlap between consecutive tracks, considering the typical single track width of $w_t \sim 1$ mm observed in the considered conditions.

The experimental conditions of the campaign are represented in the space of process parameters in Figure 8. Images of the realized samples are reported for each condition. From a qualitative point of view, the parts were deposited with a cubic shape as expected, except for condition C9: the latter represented an evident process failure, with an irregular shape and a significantly lower final height. Moreover it can be observed that the conditions at higher scanning speed showed more regular surfaces for the lateral walls, with a reduction of the debris attachment effect.

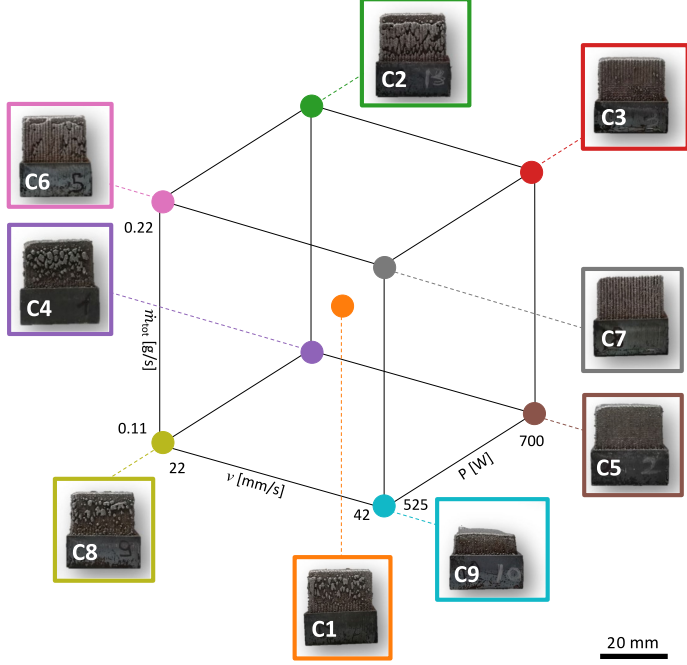


Figure 8: Representation of the experimental conditions in the space of varied process parameters. A side-view image of deposited sample over its substrate is reported for each condition.

The deposition track shape was analyzed for samples in few significant process conditions, for a qualitative check of the model hypotheses and of the dimensional measurements. Accordingly, the cuboids were cut along the growth direction to highlight the cladding structures. The cross sections were polished and chemical etched using a solution of distilled water, hydrochloric acid, and nitric acid for 10s. The shapes of the deposition layers and tracks along the cross sections were analyzed using an optical profilometer (Mitutoyo Quick Vision ELF QV-202).

5. Results

5.1. Mass measurements

The deposition mass was measured in real-time during the process by means of the load cell system. The initial mass offsets given by substrates and supports were subtracted from the load cell readouts. Each series was grouped by track and layer number, whose intervals were identified by acquiring the process laser emission with the monitor photodiode. The data have been smoothed using a 2-nd order low-pass filter with 5 layer cutoff, to suppress intra-layer variability related to the robot positioning vibrations. Indeed the current study is focused on the overall behavior of the bulk deposition process, not on the single layer spurious fluctuations. Finally, the data of each group of 3 replicates have been averaged point-by-point to extract the mean trend for each experimental condition. The results for the average deposition mass \bar{m}_{dep} are reported in Figure 9(a) as a function of layer number.

Conversely to the substrate load cell, the hopper sensor readout showed big oscillations, probably caused by vibrations induced by the robot movements. Accordingly, the acquisitions of the lost powder were used just to check its final mass value, confirming that inefficiency is mainly determined by the powder which is not captured by the melt pool, falling from the deposition substrate and being collected by the hopper. Therefore the powder catchment efficiency of each layer was calculated using Eq. (2) by differentiating \bar{m}_{dep} , assuming the total mass flow rate $\dot{m}_{tot} = \dot{m}_{dep} + \dot{m}_{lost}$ as a constant parameter known from a preliminary

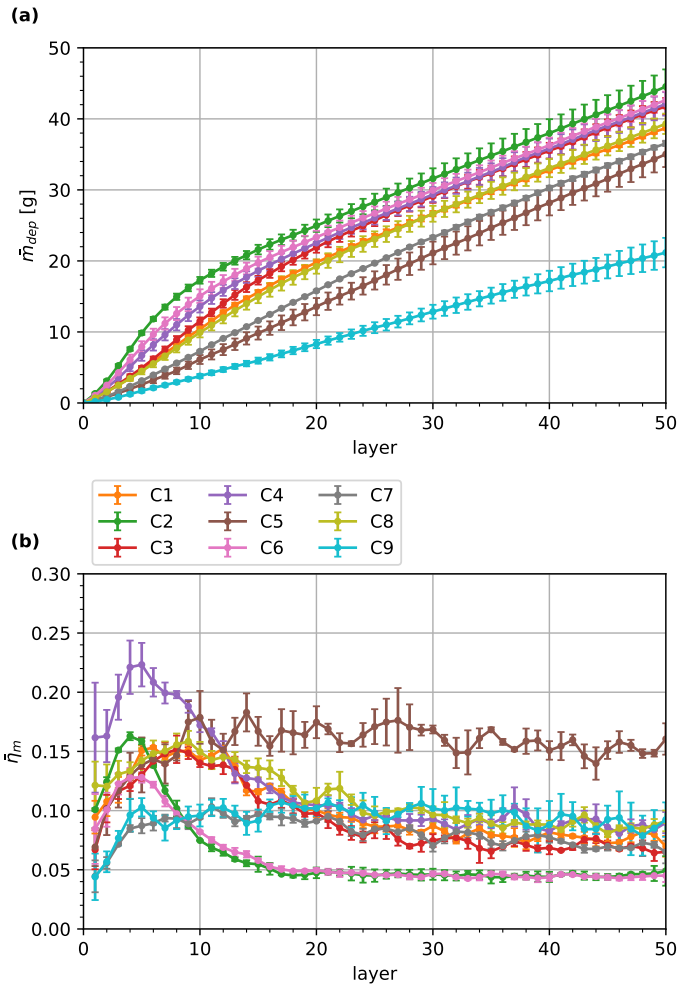


Figure 9: (a) Average deposition mass measured as a function of layer number, grouped by experimental condition. (b) Overall powder catchment efficiency calculated from the weight measurements, including the path strategy intrinsic inefficiency. Error bars represent standard deviations within replicates for each process condition. Curves are low-pass filtered with a 5 layer cut-off.

offline calibration of the mass flow rate provided by powder feeder. The corresponding powder catchment efficiency curves are reported in Figure 9(b).

The experimental results show that, in most conditions, the trend of \bar{m}_{dep} undergoes a slope change within the first ~ 10 layers. After that, the deposition mass curves grow almost linearly with similar slopes, apart from condition C9 which departs with a clearly slower deposition rate. This behavior reflects on efficiency, with $\bar{\eta}_m$ reaching its maximum value $\lesssim 0.25$ within the initial layers for almost every condition. After such initial transient $\bar{\eta}_m$ stabilizes at lower values between 0.05 and 0.15, with an essentially constant trend for all conditions.

A first preliminary analysis is proposed considering the stationary powder catchment efficiency as response variable, measured as $\bar{\eta}_m$ averaged over the last 10 layers. The main effects and interaction plots of the response variable are reported in Figure 10. The main effects plot implies that the strongest influence on $\bar{\eta}_m$ for the last layers derives from the delivered powder mass flow rate, \dot{m}_{tot} ; nevertheless both processing laser power P and transverse scanning speed v affect the powder catchment efficiency in the stationary condition. While an increase in P and v reflects in a greater efficiency, higher values of \dot{m}_{tot} appear to induce a lower $\bar{\eta}_m$. Moreover the interaction plots suggest interactions between processing laser power and deposition scanning speed ($P \cdot v$) and between processing laser power and the delivered powder mass flow rate ($P \cdot \dot{m}_{tot}$). On the other hand, no strong interactions are expected between the deposition scanning speed, v and the delivered powder mass flow rate, \dot{m}_{tot} . The respective analysis of variance (ANOVA) showed that all the parameters P , v , and \dot{m}_{tot} and their second order interactions are significant; the detailed results are omitted for the sake of brevity.

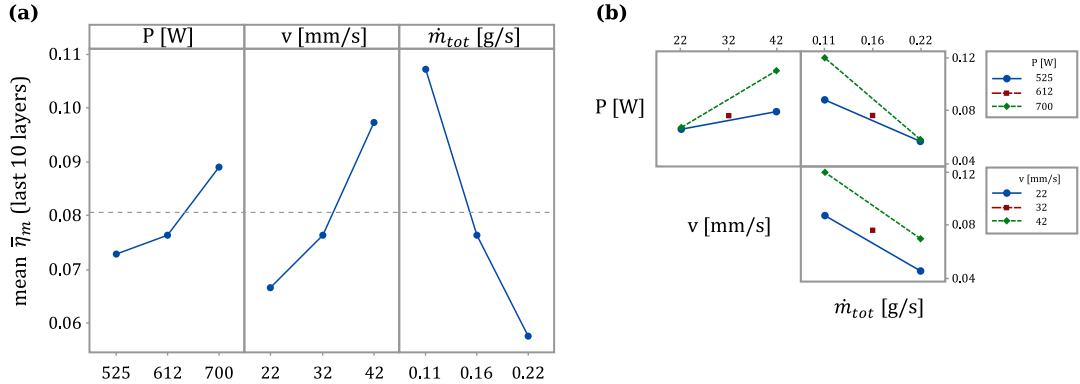


Figure 10: Main effects plot (a) and interaction plots (b) for the mean $\bar{\eta}_m$ in the last 10 layer, to highlight the role of process parameters on the overall powder catchment efficiency in a stationary regime. Each point represents the average for all the experimental runs taken at the corresponding parameter value. The horizontal dashed gray line represents the average over all the experimental runs.

The analysis reported here can be interesting from a technological point view, since the final user is typically interested to the overall efficiency, measured as the deposit mass over the total deposition time in its steady state. However it must be stressed that $\bar{\eta}_m$ is not relevant for a direct description of the deposition process physics, since it is comprehensive of losses related to the deposition strategy and, in particular, its value is reduced by the presence of intervals along the deposition path where the processing laser emission is disabled. Moreover, the key role of standoff distance has not been taken into account at this preliminary stage. As it will be discussed in the following sections, the depositions in the different experimental conditions stabilize at different standoff distance values, hence in different conditions of laser-powder interaction and height self-regulation.

5.2. Height measurements

The standoff distance was measured in real-time as a function of deposition time by means of the coaxial triangulation system. The synchronous logging of the robot coordinates was used to identify the deposition

head position, thus to extract the track and layer numbers. This allowed to reconstruct the three-dimensional structure of the deposited samples. An example of acquisition is represented in Figure 11. It can be seen that the standoff distance departs from its initial nominal value $S_0 = 12$ mm after the first layers, with the color scale gradient showing an initially faster deposition growth and a final height mismatch of about 3 mm. The track-to-track and layer-to-layer variability can be ascribed to inaccuracies in the robot positioning and to laser head vibrations. These were quantified from the logs of the acquired robot axis encoders: the average standard deviation for the robot height within each layer was of the order of 70 μm ; moreover, the robot height increment exhibited a standard deviation of about 30 μm relatively to its nominal value 0.2 mm, with peak mismatches up to 0.1 mm. Clearly these mechanical inaccuracies reflect on the optical distance measurement, influencing also the process conditions related to standoff distance, as it will be discussed while commenting on the process stability.

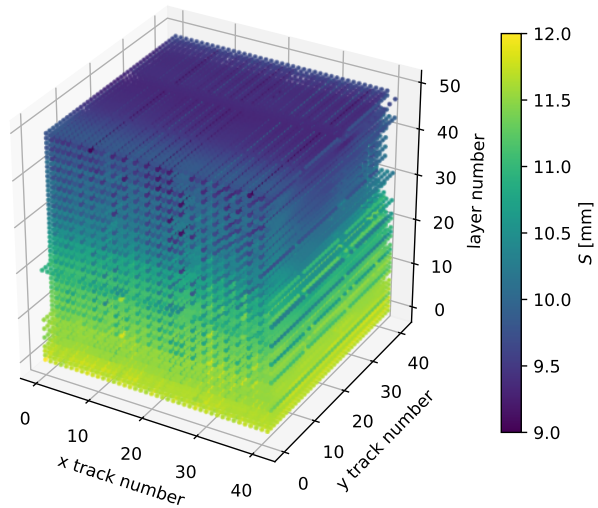


Figure 11: Three-dimensional representation of a deposited sample for the experimental condition C5. Color scale represents the measured standoff distance. The structure is composed of 50 layers with 42 tracks each.

Similarly to the analysis of \bar{m}_{dep} , the data sets of the mean standoff distance have been low-pass filtered and averaged over the 3 replicates to suppress layer-to-layer fast fluctuations. The results for the mean standoff distance \bar{S} in the different experimental conditions are reported in Figure 12(a). The curves highlight that \bar{S} departs from its initial value $S_0 \simeq 12$ mm with a slope which depends on the process condition. Apart from condition C9, all the curves show a reduction in the standoff distance, hence an actual deposit growth which is faster than the designed height. For almost every condition a stationary standoff distance is reached after the first ~ 20 layers, with the final values of \bar{S} ranging between 7 mm and 9 mm, where the process enters in the self-stabilized regime for the deposition height growth.

The average layer height \bar{h} has been calculated differentiating the standoff distance, following Eq. (13). The results are reported in Figure 12(b). For almost every condition the layer height undergoes an initial positive mismatch relatively to the robot increment along the build direction, fixed to $r_z = 0.2$ mm. Such condition corresponds to a deposition height which grows faster than the programmed robot path, with \bar{h} reaching values up to 0.8 mm for condition C2, 4 times r_z . After such transient the layer height tends to r_z , hence matching the robot height increment in the self-regulated regime. The only exception is C9, where a different behavior is observed, with the layer height being always slightly below r_z : this corresponds to process instability, with a departure towards bigger standoff distance values.

Figure 13 reports a cross-section acquired by means of optical microscopy for a sample deposited in condition C2. Horizontal lines are superimposed to the image to represent the average layer height measured

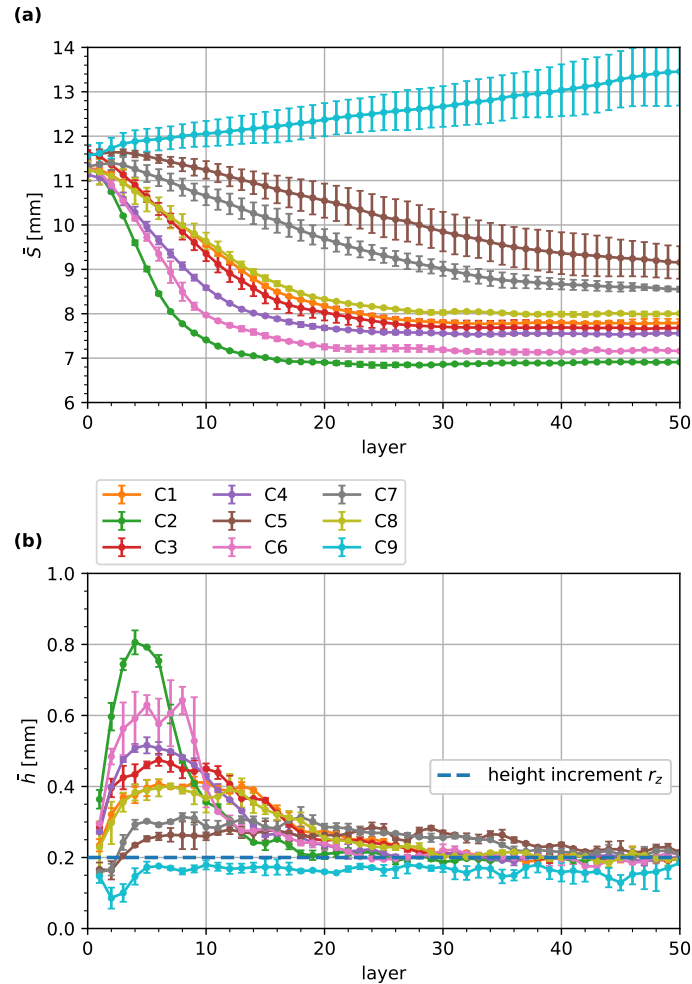


Figure 12: (a) Average standoff distance measured as a function of layer number, grouped by experimental condition. (b) Layer height calculated from the standoff distance differentiation. The robot height increment $r_z = 0.2$ mm is highlighted with a dashed line. Error bars represent standard deviations within replicates. Curves are low-pass filtered with a 5 layer cut-off.

with inline triangulation. Vertical lines having horizontal spacing equal to the nominal robot transverse increment $r_x = 0.45$ mm are also reported. The picture provides a qualitative validation for the coaxial triangulation measurements for the description of the layer height during the deposition. Moreover, as it can be observed from the image magnifications, the deposition track shape changes significantly during the different deposition stages. Within the initial, unstable, layers the tracks are taller and strongly inclined, with the presence of pores caused by lack of fusion; conversely, the final self-regulated regime corresponds to a more regular track pattern, with the layer height matching the robot height increment $r_z = 0.2$ mm. These observations support the validity of the approximations which were introduced in Eq. (8) regarding the track cross-section geometry for a bulk deposition. As a matter of fact, if the deposit is filled and pores are negligible, the average cross-section area can be calculated assuming an effective rectangular track, whose height and width are set by the average layer height and by the robot transverse increment, respectively.

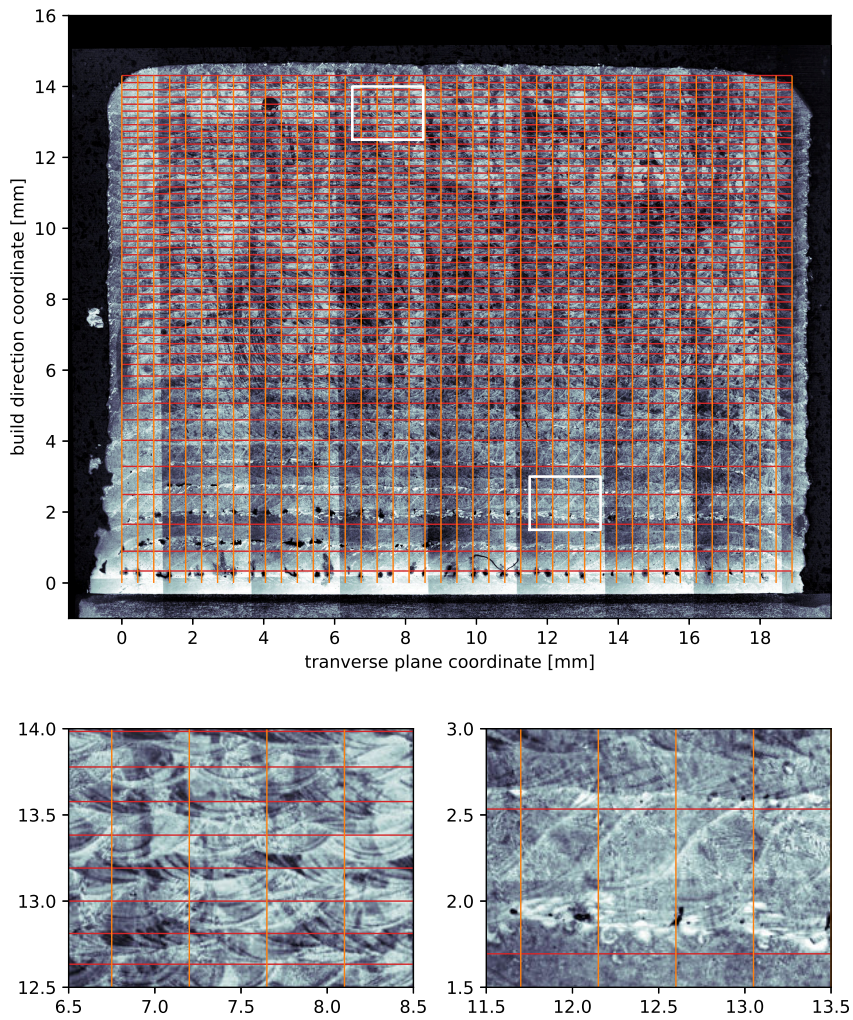


Figure 13: Cross-section along the build direction for a sample in process condition C2. Horizontal lines (orange) represent the average layer height values measured with optical triangulation. Vertical lines (red) represent the nominal robot path transverse increment $r_x = 0.45$ mm. In the bottom, two magnifications are reported to highlight single tracks in different characteristic zones, at the beginning and at the end of the deposition.

5.3. Powder catchment efficiency

The geometrical definition of powder catchment efficiency $\bar{\eta}_h$ can be calculated from the layer height measurements using Eq. (9). The results are reported in Figure 14(a). They show that efficiency is typically varied between 0.08 and 0.4, with an initial transient that follows the behavior which was already observed for $\bar{\eta}_m$ in Figure 9(b). The efficiency stabilizes after about 20 layers, with C5 being the most efficient condition, while C6 and C2 correspond to the least efficient ones.

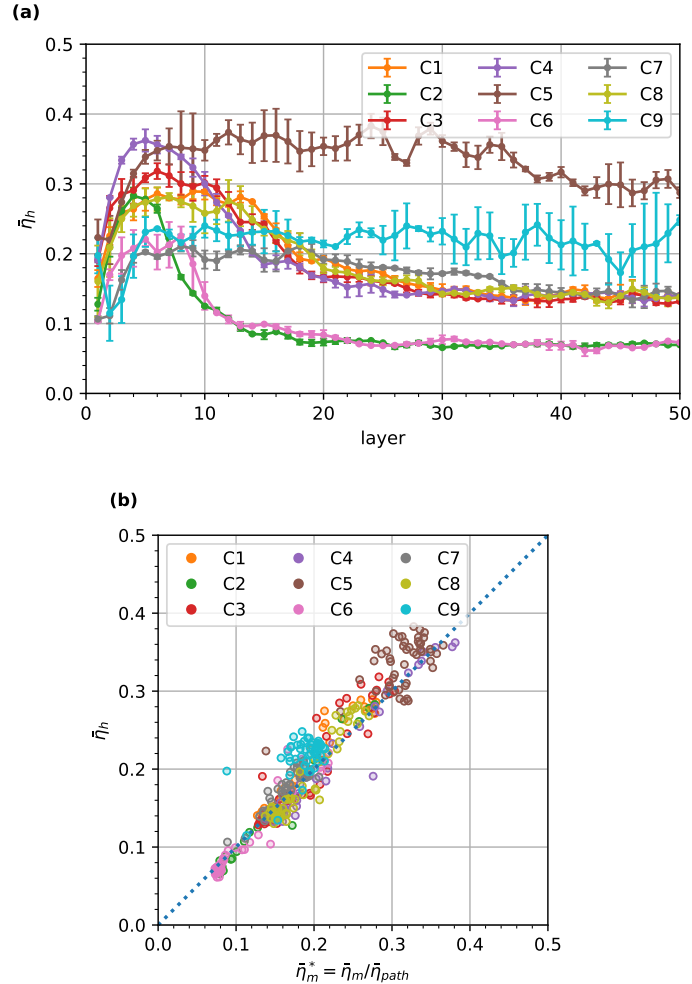


Figure 14: (a) Geometrical definition of powder catchment efficiency calculated by means of the layer height model. (b) Scatter plot for the comparison between the effective powder catchment efficiency and its indirect geometrical measurement; the diagonal line highlights the expected behavior. Each point represents the average efficiency for a single layer.

For a quantitative comparison between $\bar{\eta}_h$ and the powder catchment efficiency $\bar{\eta}_m$ obtained from direct mass measurements, the latter must be corrected to isolate the effects related to the deposition process only. Indeed, the definition of the overall powder catchment efficiency $\bar{\eta}_m$ introduced in Eq. (2) includes an efficiency component $\bar{\eta}_{path}$ determined by the deposition geometry and by the robot dynamical parameters. Such path strategy term has been estimated from the robot logs as the ratio between the sum of laser emission intervals over the whole deposition time, following the definition of Eq. (3). The average values of $\bar{\eta}_{path}$ depend on the scanning speed: 0.50 for $v = 42$ mm/s, 0.55 for $v = 32$ mm/s, and 0.59 for $v = 22$ mm/s.

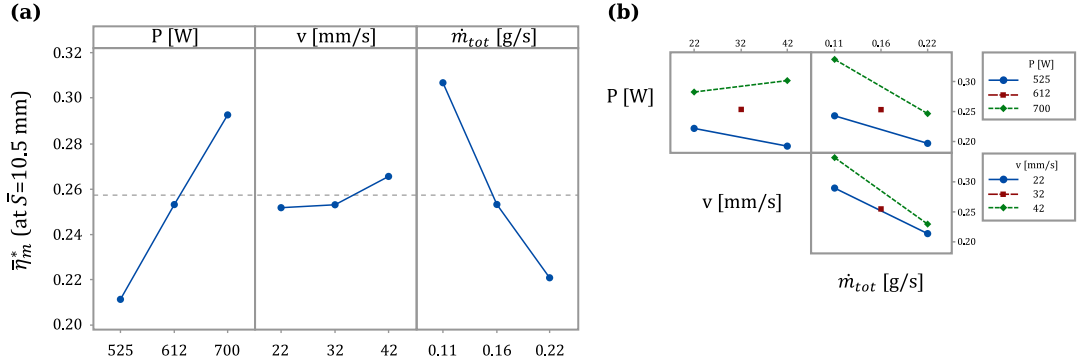


Figure 15: Main effects plot (a) and interaction plots (b) for the effective powder catchment efficiency as a function of varied parameters, interpolated at the common standoff distance $\bar{S} = 10.5$ mm. Each point represents the average for all the experimental runs taken at the corresponding parameter value. The horizontal dashed gray line represents the average over all the experimental runs. The unstable condition C9 was excluded from the analysis since it never crosses $\bar{S} = 10.5$ mm.

This means that a remarkable powder fraction equal to $1 - \bar{\eta}_{path}$ is lost during the robot position settlement, when the laser emission is turned off.

Although the inefficiency introduced by $\bar{\eta}_{path}$ is important from the point of view of the overall deposition costs, this is essentially determined by technical reasons and it is not relevant for the comprehension of the deposition process physics. Therefore the effective powder catchment efficiency can be calculated as $\bar{\eta}_m^* = \bar{\eta}_m / \bar{\eta}_{path}$ as introduced in Eq. (4). The experimental values of $\bar{\eta}_m^*$ and $\bar{\eta}_h$ are compared in the scatter plot of Figure 14(b). It can be seen that there is a good correspondence between the two efficiency measurements. Most of the experimental points lay close to the correspondence diagonal, with a Pearson correlation coefficient equal to 0.97. This means that powder catchment efficiency is actually linked to the deposition height as it was derived in the layer height model, demonstrating that the powder catchment efficiency can be conveniently probed by means of an indirect geometrical measurement.

The results for the effective powder catchment efficiency $\bar{\eta}_m^*$ have been analyzed to identify the influence of the deposition parameters on the process physics. Differently from the results reported in Figure 15, here the efficiency is analyzed at constant standoff distance S . This allows to suppress the strong dependence of the laser-powder interaction on S , which was discussed in the model for η_{int} in Eq. (15). Accordingly, $\bar{\eta}_m^*$ has been interpolated at the same standoff distance value for all the experimental curves: $\bar{S} = 10.5$ mm has been conveniently chosen as test point since such value was crossed for all the conditions after few initial layers and before self-stabilization. The substrate thermalization transients expected at the beginning are therefore avoided, and data comparison can be performed with consistency. The unstable condition C9 was excluded from the analysis. The interpolated $\bar{\eta}_m^*$ is reported in Figure 15 as a function of the varied parameters. The main effects plot shows that there is an influence for the laser power and the powder flow rate on efficiency: $\bar{\eta}_m^*$ grows with P , while it decreases with \dot{m}_{tot} . The ANOVA table, omitted for brevity, showed that only these two parameters are significant. Such results are in agreement with the predictions for the theoretical powder catchment efficiency η_{th} introduced in Eq. (18), essentially confirming the validity of the model hypotheses. Analogously, the lack of influence of v on $\bar{\eta}_m^*$ is in accordance with the dependence of η_{th} on the ratio P/\dot{m}_{tot} , i.e. on the quantity of energy available for a given amount of delivered powder mass. Indeed the scanning speed is relevant for the initial transient caused by thermal accumulation and temperature rise during the layers at the beginning, but in the stationary condition it affects equally the energy and powder concentrations, and its effect on the effective powder catchment efficiency can be neglected in a first-order approximation.

5.4. Effects of standoff distance on efficiency and height growth

The dependence of powder catchment efficiency on standoff distance is highlighted in Figure 16(a), where $\bar{\eta}_h$ is plotted as a function of \bar{S} . Apart the transient around the initial standoff distance $S_0 \simeq 12$ mm,

attributable to thermal stabilization effects of the substrate, the process tends to lower efficiencies when it enters in the self-regulated regime, occurring at smaller standoff distance values. The only exception is condition C9, which departs toward bigger \bar{S} values, hence to process instability. The highest efficiency in the self-regulated regime is observed for condition C5, which also corresponds to the smallest standoff distance mismatch relatively to its initial reference value S_0 during process stabilization.

In the proposed model, the theoretical powder catchment efficiency η_{th} was defined in Eq. (18) from the process parameters P and \dot{m}_{tot} , with \dot{m}_{tot} determining the saturation melting power P_0 introduced in Eq. (16). Moreover η_{th} depended on the standoff distance S as a consequence of the variable interaction area A_{int} , which can be calculated from Eq. (24) knowing the powder and laser beam configurations. These were characterized as previously described while presenting the experimental setup. Therefore, in principle the theoretical powder catchment efficiency η_{th} can be calculated as a function of \bar{S} for each process condition.

It must be remarked that a geometrical correction factor c_g was implicitly included in the definition of η_{th} , introduced in Eq. (23). This was necessary to take into account of the approximations assumed in the discussion, in particular regarding the laser-powder interaction region and spatial beam distributions. Moreover, it can be expected that c_g is influenced by the specific deposition geometry and strategy, determining the effects of thermal accumulation and melt pool evolution during the deposition. Accordingly c_g was used to calibrate the semi-empirical model to the experimental efficiency curves of Figure 16(a), by fitting η_{th} against the corresponding experimental $\bar{\eta}_h$ series. The optimal correction factor was determined as $c_g = 2.19 \pm 0.17$ by averaging the fit results for all the process conditions. The correction factor value $c_g > 1$ suggests that the model underestimates the effective laser-powder interaction region, probably due to the approximations considered in the laser energy and powder uniform spatial distributions. Reasonably c_g can be explained in terms of a melt pool which is bigger than the laser spot, e.g. considering an elongated melt pool, whose cue plays a relevant role in the powder catchment.

The curves of η_{th} calculated with the common value of c_g found from calibration are reported in Figure 16(b). It can be observed that, although second-order corrections might be required for a quantitatively precise matching, the efficiency model is consistent with the measurements of Figure 16(a). Clearly the initial efficiency transients observed experimentally around S_0 are not reproducible, since the simulated efficiency curves assume a stationary thermal condition.

From Eq. (18) it follows that the theoretical powder catchment efficiency is determined by two independent quantities, S and the ratio P/P_0 , which reduces to P/\dot{m}_{tot} making explicit for convenience the dependence on the considered variable process parameters. Therefore η_{th} can be described in a bi-dimensional space as shown in Figure 16(c). The color map shows a high efficiency region for big values of P/\dot{m}_{tot} around $S_0 = 12$ mm, where the laser intensity is sufficient to melt more efficiently the available powder flux. Moreover efficiency decreases with S , due to the reduction of the laser-powder beam interaction. In such representation each process condition lays on a horizontal line set by the values of P and \dot{m}_{tot} , determining the efficiency evolution as a function of the variable standoff distance.

The self-regulating behavior is evident in Figure 17(a), where the measured layer height \bar{h} is plotted as a function of the average standoff distance \bar{S} . It can be seen that, starting from the initial standoff distance $S_0 \simeq 12$ mm, a positive height mismatch brings the deposition in the self-regulation regime, i.e. at lower \bar{S} values. The corresponding height variability is influenced by the process condition. Specifically, C2 shows the bigger variability and smaller final standoff distance, while C5 is the condition which closely matches the robot height increment r_z , ending close to the initial standoff distance S_0 . Remarkably, the reduced layer height variability observed for condition C5 is associated also to a high powder catchment efficiency, as commented for Figure 16(a). Only for condition C9 the process deviates to the unstable regime, with $\bar{h} < r_z$.

The theoretical layer height is calculated using Eq. (25) as a function of standoff distance in Figure 17(b), keeping the value of $c_g = 2.19$ which was previously determined. It can be seen that the results for h_{th} are in good accordance with the experimental curves of Figure 17(a), neglecting the transient around the initial standoff distance S_0 caused by thermal effects before the substrate temperature stabilization. In Figure 17(c) h_{th} is plotted as a function of two independent quantities, similarly to the treatment of η_{th} : the standoff distance S (horizontal axis) and a combination of the parameters \dot{m}_{tot} , v and P (vertical axis), which can be obtained from Equations (25) and (18). Each parameter combination determines a process

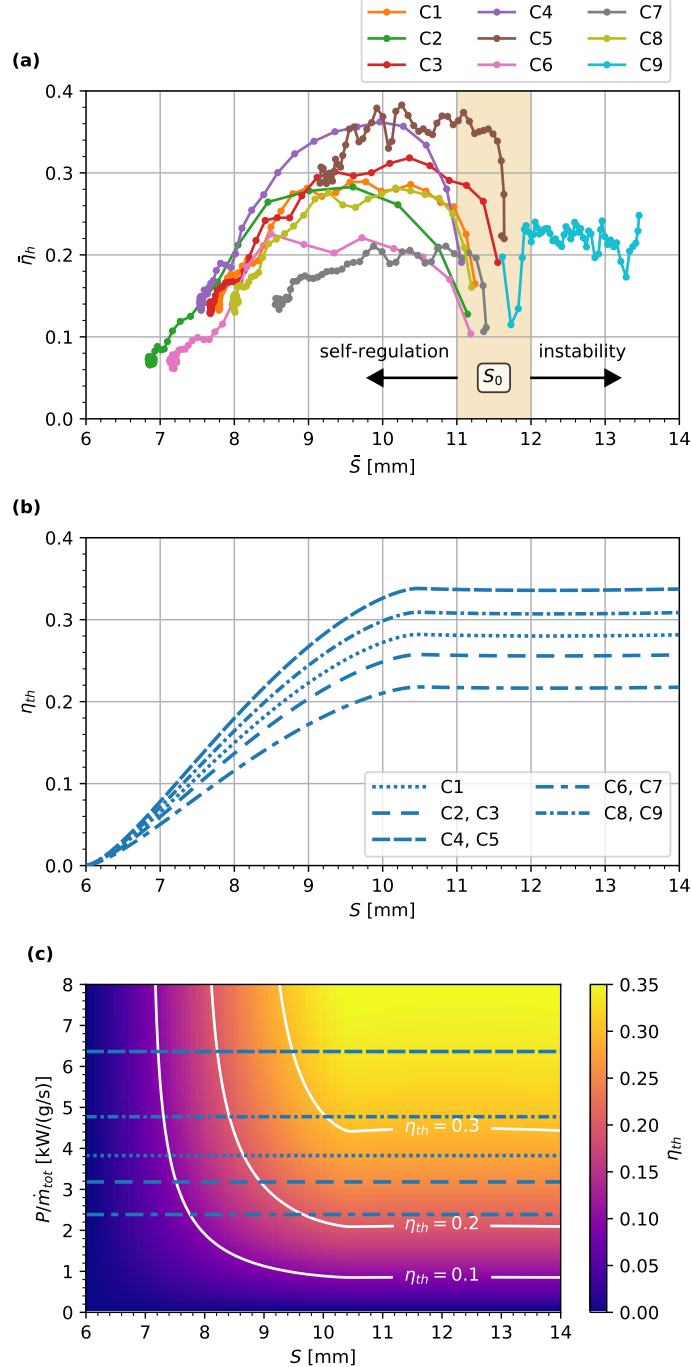


Figure 16: (a) Experimental powder catchment efficiency plotted as a function of standoff distance for the different experimental conditions; starting around the nominal value S_0 in the shaded interval, the self-regulated regime is observed when moving to smaller standoff distance values. Error bars are omitted for simplicity. (b) Theoretical powder catchment efficiency calculated as a function of standoff distance; the curves are calculated considering a correction factor $c_g = 2.19$. (c) Color map of the theoretical powder catchment efficiency, represented as a function of standoff distance (horizontal axis) and of a process parameter combination (vertical axis); the equivalent experimental conditions are reported as horizontal lines.

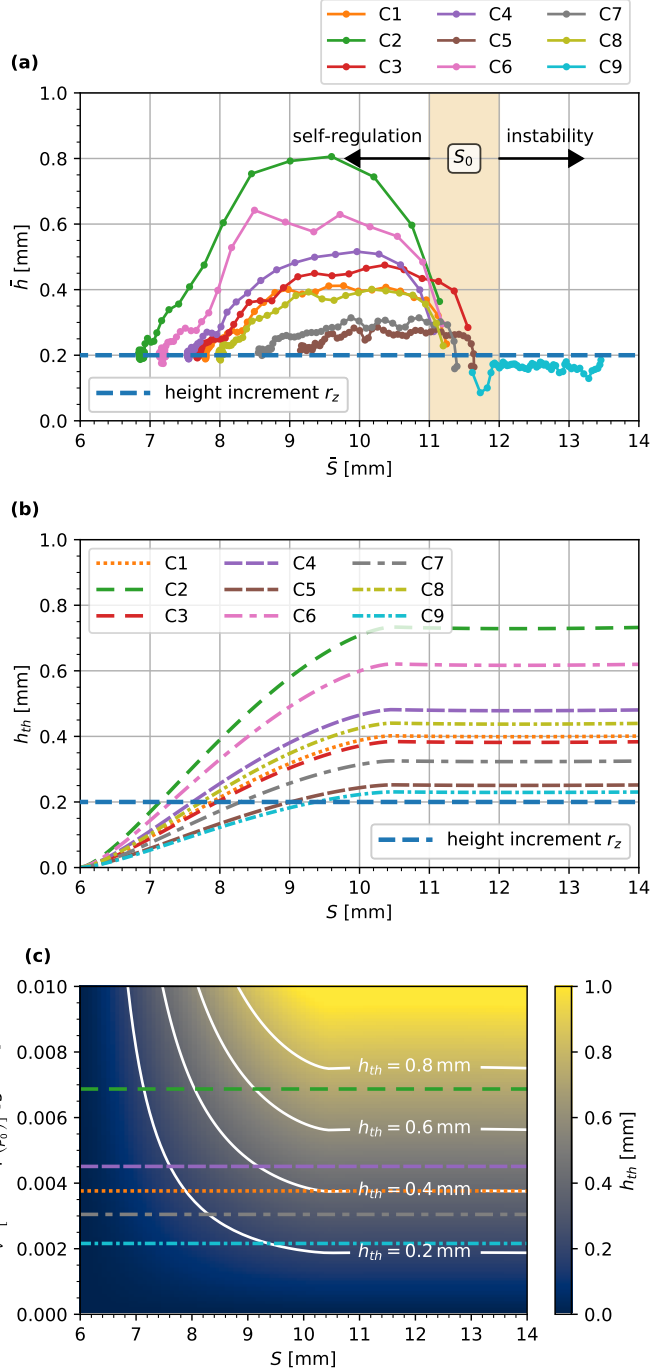


Figure 17: (a) Experimental layer height plotted as a function of standoff distance for the different experimental conditions; starting around the nominal value S_0 in the shaded interval, the self-regulated regime is observed when the layer height mismatch is greater than the robot height increment $r_z = 0.2$ mm, highlighted with a dashed line. Error bars are omitted for simplicity. (b) Theoretical layer height calculated as a function of standoff distance for the considered conditions, considering a correction factor $c_g = 2.19$. (c) Color map of the theoretical layer height, represented as a function of standoff distance (horizontal axis) and of a process parameter combination (vertical axis); the values for some characteristic process conditions are reported as horizontal lines.

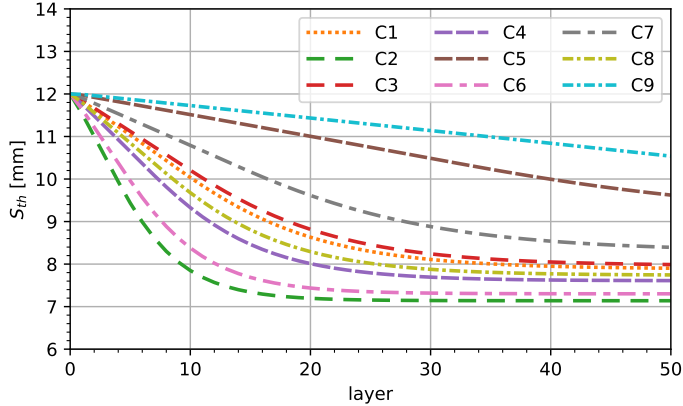


Figure 18: Theoretical standoff distance simulated with the efficiency model, calculated as a function of layer number for the considered process conditions. The simulations reproduce the self-regulation mechanism, and can be compared with the experimental curves of Figure 12(a).

condition along a horizontal line. Therefore, process self-regulation is expected to happen along the isoline of the robot height increment, where the matching condition $h_{th} = r_z$ is fulfilled, with an evolution ruled by the non-zero gradient $\partial h_{th}/\partial S > 0$.

From a different point of view, the calculation of the theoretical efficiency η_{th} allows to predict the deposition growth for each set of process parameters. This has been performed using Eq. (26) to simulate the standoff distance as a function of layer number, hence summing up the predicted layer height contributions h_{th} starting from $S_0 = 12$ mm. This is equivalent to determine the process evolution along a horizontal line of the map reported in Figure 17(c). The results corresponding to each considered experimental condition are reported in Figure 18. It can be seen that, excluding condition C9, there is a good correspondence with the experimental standoff distance curves reported in Figure 12(a). This means that the variable powder catchment efficiency, modeled in terms of process parameters and variable powder and energy distributions, allows to explain the experimental transient to closer standoff distances and lower efficiencies, hence providing a quantitatively valid interpretation for the process self-regulation and stabilization.

6. Discussion

The results for the deposition height and mass measurements showed that the powder catchment efficiency can be determined by measuring the layer height. In fact the η_m^* and η_h efficiency definitions resulted highly correlated, as evident from Figure 14(b) and predicted in Section 2.2. This confirmed the validity of the model hypotheses, stressing that these were introduced in the assumption of a stationary bulk deposition. The demonstration of η_h as a good efficiency estimator allows for the possibility of using dimensional monitoring techniques also for the study of process optimization. Coaxial triangulation is particularly interesting for the scope, since its optical probe can be easily implemented on a wide class of existing setups at a reduced cost, allowing flexibility in the deposition process monitoring, without requiring more complex and intrusive setups for the direct deposition mass measurement.

The results highlighted that the deposition height instability is mainly caused by efficiency variability. In fact the powder catchment efficiency depends on standoff distance due to the variable spatial interaction between the laser and powder beams, as shown in Figure 16(a). This allows to explain the process self-regulation. Indeed, in the considered configuration such passive stabilization mechanism is observed when the layer growth overcomes the robot height increment at the beginning, as reported in Figure 17(a). However, the standoff distance reduction reflects in a lower efficiency, acting as a negative loop feedback as predicted by the model and confirmed by experiments. This effect is ruled by the reduction of the laser-powder interaction below a characteristic standoff distance, as shown by the calculation reported in Figure 4(b). At

the end, the deposition stabilizes when the reduced efficiency brings the deposition layer height to match the robot height increment. This happens at different standoff distance values, depending on the process parameters.

Deposition self-regulation is desirable because of the corresponding process robustness and geometrical accuracy enhancement. However this is in concurrency with powder catchment efficiency. A compromise between the two aspects must be taken into account. Moreover, stabilization can be reached after a transient in the standoff distance, hence a departure from the geometrical design. Therefore the choice of the initial process parameters is particularly important for optimizing powder catchment efficiency, process stability, growth regularity, and part accuracy. The semi-empirical model for η_{th} provides a powerful tool for this task. Such model was developed assuming a stationary bulk deposition, characterized by multiple layers with a high track number $N_t \gg 1$, neglecting possible second-order effects determined by the specific deposition geometry and uncontrolled thermal drifts. Indeed, after a preliminary model calibration through c_g , the theoretical efficiency map of Figure 16(c) allows to identify the most efficient parameter combination, related to the ratio between laser power and delivered powder rate, and the respective initial standoff distance. Analogously, the theoretical layer height map of Figure 17(c) allows to identify the stability conditions depending on the required resolution, i.e. fixing the robot height increment and the scanning speed such that $h_{th} > r_z$. A wise choice takes the combination of initial standoff distance and robot height increment which lays close to the layer height predicted in the corresponding map region. This means that the process will stabilize soon, without varying significantly from the initial standoff distance and from the designed geometry, while maintaining an optimal efficiency. Moreover the isoline $h_{th} = r_z$ should be crossed transversely during the standoff distance evolution to reach stability, in a condition where the gradient $\partial h_{th} / \partial S > 0$ is maximized to guarantee a robust and fast convergence.

For the considered experimental campaign the best choice seems to be represented by condition C5, which is both efficient and characterized by a height growth that closely follows the programmed robot path. In fact, for C5 the energetic efficiency term η_{en} is maximum, since the high laser power and low powder mass flux guarantees a high melting rate, hence low powder losses. Moreover, the combination of these parameters with the respective scanning speed guarantees a layer height growth that almost matches the robot height increment at the initial standoff distance, hence process stability and deposition regularity. However it must be noted that, even in the most convenient standoff distance condition, the powder catchment efficiency is limited to less than 0.4 by the partial interaction between the laser and powder beams, expressed by η_{int} and calculated in Figure 4(b). This is given by the laser spot size, which is smaller than the powder beam spot to achieve a good transverse resolution.

The model can be used for an open-loop process optimization, since it allows to predict the deposition growth as shown in Figure 18. Indeed, the knowledge of the expected deposition growth can allow for a quantitative preliminary correction of the geometrical model to meet the design requirements. For example, this might be performed by compensating the deposition height mismatch in the programmed robot path, once the choice of the initial process parameters have been performed. Moreover the threshold between self-stabilized and unstable growth can be also identified from the model, reducing the risk of deposition failures and wastes. This can represent a great advantage during the component design and realization, reducing the number of preliminary tests and manual operations required for the parameter optimization.

As a final comment regarding the limits of the proposed approach, it must be observed that the model predicts very similar layer height trends for C5 and C9: however the latter exhibited instability in experiments. This can be interpreted considering that C9 lays very close to the minimum stability condition for the chosen robot height increment, represented by the horizontal part of the isoline $h_{th} = r_z$ in the layer height map, where $\partial h_{th} / \partial S \sim 0$. Further investigations should be required for a precise description around the stability threshold. Moreover, the robot positioning inaccuracies discussed while presenting Figure 11 may play an important role in these borderline conditions, since the standoff distance vibrations can eventually bring the process to an actual region of instability. This suggests that a reasonable safety margin should be considered relatively to the stability threshold in the process parameter choice, in order to reduce the effects of such kind of uncontrolled technical aspects.

7. Conclusions

This work provided a systematic investigation for a greater understanding of the layer height variations and self-stabilization in LMD. The work shows the development of modeling and experimental methods to evaluate the powder catchment efficiency inline the process. For this task a load cell setup was constructed and employed during the LMD of AISI 316L stainless steel with a robotic deposition system, while a coaxial triangulation device measured the deposition height during the process. The results confirm the link between powder catchment efficiency and height variations during the process. The main outcomes of the work are as follows.

- The powder catchment efficiency mainly relies on the balance between the laser power and the delivered powder mass flow rate. The resulting layer height depends on the interplay between powder catchment efficiency, delivered mass flow rate, and scanning speed. Considering a geometric interaction zone as proposed in the analytical model, the laser beam should provide the required energy to fuse the deposited powder. Accordingly, the standoff distance plays a crucial role in the determination of the powder catchment efficiency, hence of the layer height, because of the variable laser-powder interaction. For the considered system the maximum achievable efficiency was limited by the partial overlap between laser and powder beams.
- The initial standoff distance defines the initial geometrical conditions that determine the powder and laser beam interaction zone. The deviations from this initial condition depends on the capacity of the laser to melt the delivered powder, determined on the process parameters. For each explored parameter set, the self-stabilization condition differed in the final standoff distance and powder catchment efficiency, while the layer height increment could be matched. Such passive stabilization mechanism is associated to an efficiency reduction. The only condition that could not provide a self-stabilization of height was associated to a combination of low laser power, low powder flow rate, and high scanning speed, which did not guarantee a sufficient layer growth to match the robot height increment.
- The powder distribution, hence the nozzle design, plays a critical role on the selection of the process parameters, especially of the initial standoff distance. Although limited to the experimented nozzle type, the work showed that the process parameters can be adapted to a higher powder catchment efficiency for different parameter sets. This can be useful not only for developing higher material usage in the process, but also for maintaining a stable deposition when thin tracks may be required, enhancing the geometrical accuracy and process robustness.
- The use of a load cell system is a straightforward approach to measure the powder catchment efficiency, and hence the process stability. However its use in larger constructions is invasive and difficult. Instead, the coaxial optical triangulation system was proven to be sufficient for estimating the powder catchment efficiency through an analytical model, despite its several strong assumptions. Hence coaxial triangulation can be used also for process comprehension, along with its main use as an inline height measurement tool.
- The work shows that through the use of the described experimental and modeling framework, process maps can be generated to establish the link between the powder catchment efficiency and the standoff distance. This can be potentially integrated to path planning during the generation of the computer aided manufacturing (CAM) code. Moreover the model can be applied to train the response of closed-loop control systems to obtain a regular deposition growth, e.g. integrating the dimensional measurement by means of coaxial triangulation with a feedback correction on the process parameters such as laser power, scanning speed, or powder flow.

Although this work provides several insights for a better understanding of the LMD process physics, several other aspects remain open. The tested conditions were characterized by an overall low powder catchment efficiency in order to assess parameter sets that provided better geometrical precision rather than high deposition rates. The approach should be further applied to such high deposition conditions. The

developed analytical model is dependent on the nozzle type, which should be extended to coaxial nozzles as well. Finally, the model does not take the nozzle wear into account, which can manifest in longer use combined with high powder mass flow. In these cases, the deviations from the expected efficiency levels can be an alarm for indicating nozzle related issues.

Acknowledgments

The authors gratefully acknowledge Mr. Riccardo Caccia for his support during the experimental work. Mr. Eligio Grossi is acknowledged for his support in the design of the electronic acquisition setup, Mr. Stefano Mutti for his support in the realization of the communication software with robot system. The authors would like to thank the BLM Group for the longstanding collaboration during the LMD cell development. The project presented in this paper has been funded with the contribution of the Autonomous Province of Trento, Italy, through the Regional Law 6/99 (Project LT 4.0). This work was supported by European Union, Repubblica Italiana, Regione Lombardia and FESR for the project MADE4LO under the call “POR FESR 2014-2020 ASSE I – AZIONE I.1.B.1.3”.

References

- [1] A. Dass, A. Moridi, State of the Art in Directed Energy Deposition: From Additive Manufacturing to Materials Design, *Coatings* 9 (7) (2019) 418. doi:10.3390/coatings9070418.
- [2] T. DebRoy, H. L. Wei, J. S. Zuback, T. Mukherjee, J. W. Elmer, J. O. Milewski, A. M. Beese, A. Wilson-Heid, A. De, W. Zhang, Additive manufacturing of metallic components – Process, structure and properties, *Progress in Materials Science* 92 (2018) 112–224. doi:10.1016/j.pmatsci.2017.10.001.
- [3] J. M. Flynn, A. Shokrani, S. T. Newman, V. Dhokia, Hybrid additive and subtractive machine tools – Research and industrial developments, *International Journal of Machine Tools and Manufacture* 101 (2016) 79–101. doi:10.1016/j.ijmachtools.2015.11.007.
- [4] K. Shah, I. U. Haq, S. A. Shah, F. U. Khan, M. T. Khan, S. Khan, Experimental Study of Direct Laser Deposition of Ti-6Al-4V and Inconel 718 by Using Pulsed Parameters, *The Scientific World Journal* 2014 (2014) 841549. doi:10.1155/2014/841549.
- [5] A. Saboori, A. Aversa, G. Marchese, S. Biamino, M. Lombardi, P. Fino, Application of Directed Energy Deposition-Based Additive Manufacturing in Repair, *Applied Sciences* 9 (16) (2019) 3316. doi:10.3390/app9163316.
- [6] F. Bruzzo, G. Catalano, A. G. Demir, B. Previtali, Surface finishing by laser re-melting applied to robotized laser metal deposition, *Optics and Lasers in Engineering* 137 (2021) 106391. doi:10.1016/j.optlaseng.2020.106391.
- [7] N. Shamsaei, A. Yadollahi, L. Bian, S. M. Thompson, An overview of Direct Laser Deposition for additive manufacturing; Part II: Mechanical behavior, process parameter optimization and control, *Additive Manufacturing* 8 (2015) 12–35. doi:10.1016/j.addma.2015.07.002.
- [8] D. Eisenbarth, F. Soffel, K. Wegener, Geometry-Based Process Adaption to Fabricate Parts with Varying Wall Thickness by Direct Metal Deposition, in: H. A. Almeida, J. C. Vasco (Eds.), *Progress in Digital and Physical Manufacturing, Lecture Notes in Mechanical Engineering*, Springer International Publishing, Cham, 2020, pp. 125–130. doi:10.1007/978-3-030-29041-2_16.
- [9] N. Pirch, S. Linnenbrink, A. Gasser, H. Schleifenbaum, Laser-aided directed energy deposition of metal powder along edges, *International Journal of Heat and Mass Transfer* 143 (2019) 118464. doi:10.1016/j.ijheatmasstransfer.2019.118464.
- [10] L. Song, V. Bagavath-Singh, B. Dutta, J. Mazumder, Control of melt pool temperature and deposition height during direct metal deposition process, *The International Journal of Advanced Manufacturing Technology* 58 (1-4) (2012) 247–256. doi:10.1007/s00170-011-3395-2.
- [11] A. Fathi, A. Khajepour, E. Toyserkani, M. Durali, Clad height control in laser solid freeform fabrication using a feedforward PID controller, *The International Journal of Advanced Manufacturing Technology* 35 (3-4) (2007) 280–292. doi:10.1007/s00170-006-0721-1.
- [12] L. Tang, R. G. Landers, Layer-to-Layer Height Control for Laser Metal Deposition Process, *Journal of Manufacturing Science and Engineering* 133 (2) (2011) 021009. doi:10.1115/1.4003691.
- [13] A. Heralić, A.-K. Christiansson, B. Lennartsson, Height control of laser metal-wire deposition based on iterative learning control and 3D scanning, *Optics and Lasers in Engineering* 50 (9) (2012) 1230–1241. doi:10.1016/j.optlaseng.2012.03.016.
- [14] M. Kogel-Hollacher, M. Streb, C. Staudenmaier, H.-I. Schneider, D. Regulin, OCT sensor for layer height control in DED using SINUMERIK® controller, in: *Laser 3D Manufacturing VII*, Vol. 11271, International Society for Optics and Photonics, 2020, p. 112710O. doi:10.1117/12.2540167.
- [15] W. U. H. Syed, A. J. Pinkerton, L. Li, A comparative study of wire feeding and powder feeding in direct diode laser deposition for rapid prototyping, *Applied Surface Science* 247 (1) (2005) 268–276. doi:10.1016/j.apsusc.2005.01.138.
- [16] C. P. Paul, S. K. Mishra, A. Kumar, L. M. Kukreja, Laser rapid manufacturing on vertical surfaces: Analytical and experimental studies, *Surface and Coatings Technology* 224 (2013) 18–28. doi:10.1016/j.surfcoat.2013.02.044.

[17] J. Lin, A simple model of powder catchment in coaxial laser cladding, *Optics & Laser Technology* 31 (3) (1999) 233–238. doi:10.1016/S0030-3992(99)00046-8.

[18] S. Cacace, V. Furlan, R. Sorci, Q. Semeraro, M. Boccadoro, Using recycled material to produce gas-atomized metal powders for additive manufacturing processes, *Journal of Cleaner Production* 268 (2020) 122218. doi:10.1016/j.jclepro.2020.122218.

[19] D. Eisenbarth, P. M. Borges Esteves, F. Wirth, K. Wegener, Spatial powder flow measurement and efficiency prediction for laser direct metal deposition, *Surface and Coatings Technology* 362 (2019) 397–408. doi:10.1016/j.surfcoat.2019.02.009.

[20] S. Donadello, M. Motta, A. G. Demir, B. Previtali, Monitoring of laser metal deposition height by means of coaxial laser triangulation, *Optics and Lasers in Engineering* 112 (2019) 136–144. doi:10.1016/j.optlaseng.2018.09.012.

[21] A. J. Pinkerton, L. Li, The significance of deposition point standoff variations in multiple-layer coaxial laser cladding (coaxial cladding standoff effects), *International Journal of Machine Tools and Manufacture* 44 (6) (2004) 573–584. doi:10.1016/j.ijmachtools.2004.01.001.

[22] G. Zhu, D. Li, A. Zhang, G. Pi, Y. Tang, The influence of laser and powder defocusing characteristics on the surface quality in laser direct metal deposition, *Optics & Laser Technology* 44 (2) (2012) 349–356. doi:10.1016/j.optlastec.2011.07.013.

[23] J. C. Haley, B. Zheng, U. S. Bertoli, A. D. Dupuy, J. M. Schoenung, E. J. Lavernia, Working distance passive stability in laser directed energy deposition additive manufacturing, *Materials & Design* 161 (2019) 86–94. doi:10.1016/j.matdes.2018.11.021.

[24] H. Tan, W. Shang, F. Zhang, A. T. Clare, X. Lin, J. Chen, W. Huang, Process mechanisms based on powder flow spatial distribution in direct metal deposition, *Journal of Materials Processing Technology* 254 (2018) 361–372. doi:10.1016/j.jmatprotec.2017.11.026.

[25] P.-Y. Lin, F.-C. Shen, K.-T. Wu, S.-J. Hwang, H.-H. Lee, Process optimization for directed energy deposition of SS316L components, *The International Journal of Advanced Manufacturing Technology* doi:10.1007/s00170-020-06113-z.

[26] Y. Huang, M. B. Khamesee, E. Toyserkani, A new physics-based model for laser directed energy deposition (powder-fed additive manufacturing): From single-track to multi-track and multi-layer, *Optics & Laser Technology* 109 (2019) 584–599. doi:10.1016/j.optlastec.2018.08.015.

[27] V. Ocelík, O. Nenadl, A. Palavra, J. T. M. De Hosson, On the geometry of coating layers formed by overlap, *Surface and Coatings Technology* 242 (2014) 54–61. doi:10.1016/j.surfcoat.2014.01.018.

[28] Z. Sun, W. Guo, L. Li, In-process measurement of melt pool cross-sectional geometry and grain orientation in a laser directed energy deposition additive manufacturing process, *Optics & Laser Technology* 129 (2020) 106280. doi:10.1016/j.optlastec.2020.106280.

[29] Y. Huang, M. B. Khamesee, E. Toyserkani, A comprehensive analytical model for laser powder-fed additive manufacturing, *Additive Manufacturing* 12 (2016) 90–99. doi:10.1016/j.addma.2016.07.001.

[30] J. Song, Y. Chew, G. Bi, X. Yao, B. Zhang, J. Bai, S. K. Moon, Numerical and experimental study of laser aided additive manufacturing for melt-pool profile and grain orientation analysis, *Materials & Design* 137 (2018) 286–297. doi:10.1016/j.matdes.2017.10.033.

[31] S. Kumar, V. Sharma, A. K. S. Choudhary, S. Chattopadhyaya, S. Hloch, Determination of layer thickness in direct metal deposition using dimensional analysis, *The International Journal of Advanced Manufacturing Technology* 67 (9) (2013) 2681–2687. doi:10.1007/s00170-012-4683-1.

[32] S. M. Thompson, L. Bian, N. Shamsaei, A. Yadollahi, An overview of Direct Laser Deposition for additive manufacturing; Part I: Transport phenomena, modeling and diagnostics, *Additive Manufacturing* 8 (2015) 36–62. doi:10.1016/j.addma.2015.07.001.

[33] A. F. H. Kaplan, G. Groboth, Process Analysis of Laser Beam Cladding, *Journal of Manufacturing Science and Engineering* 123 (4) (2001) 609–614. doi:10.1115/1.1344899.

[34] C. Zhong, T. Biermann, A. Gasser, R. Poprawe, Experimental study of effects of main process parameters on porosity, track geometry, deposition rate, and powder efficiency for high deposition rate laser metal deposition, *Journal of Laser Applications* 27 (4) (2015) 042003. doi:10.2351/1.4923335.

[35] W. M. Steen, J. Mazumder, *Laser Material Processing*, Springer London, London, 2010. doi:10.1007/978-1-84996-062-5.

[36] J. Liu, L. Li, Effects of process variables on laser direct formation of thin wall, *Optics & Laser Technology* 39 (2) (2007) 231–236. doi:10.1016/j.optlastec.2005.08.012.

[37] H. Tan, F. Zhang, X. Fu, J. Meng, G. Hu, W. Fan, W. Huang, Development of powder flow model of laser solid forming by analysis method, *The International Journal of Advanced Manufacturing Technology* 82 (5) (2016) 1421–1431. doi:10.1007/s00170-015-7481-8.

[38] S. Donadello, M. Motta, A. G. Demir, B. Previtali, Coaxial laser triangulation for height monitoring in laser metal deposition, in: *Procedia CIRP*, Vol. 74 of 10th CIRP Conference on Photonic Technologies [LANE 2018], 2018, pp. 144–148. doi:10.1016/j.procir.2018.08.066.